Mms19 promotes spindle microtubule assembly in neural stem cells through two distinct pathways

Rohan Chippalkatti[ab], **Boris Egger**[c] and **Beat Suter**[a]

[*]a: Institute of Cell Biology, University of Bern
[*]b: Graduate School for Cellular and Biomedical Sciences, University of Bern
[*]c: Department of Biology, University of Fribourg

Abstract

Mitotic divisions depend on the timely assembly and proper orientation of the mitotic spindle. Malfunctioning of these processes can considerably delay mitosis, thereby compromising tissue growth and homeostasis, and leading to chromosomal instability. Here we identified Mms19 as an important player in these processes as it promotes spindle and astral microtubule (MT) growth and consequently regulates spindle orientation and mitosis duration in *Drosophila* neural stem cells. Loss of functional *Mms19* drastically affects the growth and development of mitotic tissues in *Drosophila* larvae. We found that *Mms19* performs its mitotic activities through two different pathways. By stimulating the mitotic kinase cascade, it triggers the localization of the MT regulatory complex TACC/Msps (Transforming Acidic Coiled Coil/Minispindles, the homolog of human ch-TOG) to the centrosome. In addition, we present evidence that Mms19 stimulates MT stability and bundling by binding directly to MTs.

Introduction

The fidelity of chromosome segregation during mitotic divisions depends on the proper regulation of the structure and dynamics of spindle microtubules. Numerous mitotic factors, including different mitotic kinases and microtubule (MT) associated proteins, meticulously regulate the formation, orientation, polymerization and catastrophe of spindle MTs to ensure that the chromatids are evenly delivered to the two products of the division process, the daughter cells. Incorrect regulation of Cdks and MTs can lead to chromosomal instability and to deleterious effects on the growth and development of somatic tissues.

Mms19 was identified as a gene required for nucleotide excision repair (NER) (Prakash et al, 1979). The protein Mms19 can be found as part of the Cytoplasmic Iron-Sulfur Assembly complex (CIA), which mediates the incorporation of iron-sulfur clusters into NER proteins such as Xpd (Gari et al, 2012; Stehling et al, 2012). However, a distinct, apparently DNA repair-independent, function of *Mms19* came to light when its knock-down caused numerous mitotic spindle abnormalities in human cells (Ito et al, 2010). Downregulation of *Mms19* in young *Drosophila* embryos also revealed spindle abnormalities and chromosome segregation defects, and these phenotypes were linked to the mitotic control pathway when results by Nag and co-workers revealed that Mms19 acts as a positive regulator of the Cdk Activating Kinase (CAK) activity (Nag et al, 2018). CAK has dual roles during the cell cycle where it activates the mitotic Cdk1 during mitosis, but is recruited by Xpd to form the holoTFIIH complex during interphase (Cameroni et al, 2010). The incorporation into TFIIH causes CAK to phosphorylate an entirely different set of substrates and allows CAK to perform its functions in transcription. Nag et al proposed that Mms19 binds to Xpd during mitosis and that this binding competes with the binding of Xpd to the TFIIH subunits. Binding to Xpd could thereby release CAK to activate its mitotic targets. In this model, reduced levels of Mms19 prevent the dissociation of the Xpd-CAK complex. As a consequence, the required levels of the mitotic CAK activity are not established. Indeed, overexpressing CAK complex components in the *Mms19* loss-of-function (*Mms19^P*) background rescued the mitotic defects to a large degree (Nag et al, 2018).

87   The remarkable findings by Nag et al uncovered a novel mitotic pathway for *Mms19*. But this

88   study mostly focused on the young *Drosophila* embryo which is unusual in that all somatic

89   nuclei share a common cytoplasm in which the mitotic divisions take place. Furthermore,

90   their cell cycle consists of only S and M phases, without intervening G phases. In this situation

91   with the shared cytoplasm, the absence of Mms19 often causes microtubules emanating from

92   one spindle pole to contact the chromosomes of a neighboring nucleus. It is therefore difficult

93   to extrapolate these findings to mononuclear diploid cells that are isolated from their

94   neighbors by plasma membranes and have a full cell cycle. Furthermore, even though the

95   spindle abnormalities observed in the absence of Mms19 could be linked to compromised

96   CAK activity, the pathway acting downstream of CAK is not clearly understood. Finally,

97   overexpression of the CAK complex brought about only a partial rescue of the *Mms19^P*

98   defects, pointing towards additional, possibly CAK-independent spindle regulatory roles of

99   *Mms19*.

100

101   The objective of this study was thus to investigate the mitotic function of *Mms19* in normal

102   diploid cells with the goal of dissecting the precise pathway through which *Mms19* acts to

103   regulate mitotic spindle assembly and cell cycle progression. Because *Mms19^P* larvae lack

104   imaginal discs, we chose the larval brain neuroblasts (NBs) as a model to analyze the mitotic

105   roles of *Mms19* in cells with a full cycle. We identified several novel *Mms19* phenotypes,

106   which allowed us to pinpoint steps in the pathways that require *Mms19* activity. We found

107   that *Mms19* is required in NBs for timely progression through the cell cycle and consequently

108   for establishing normal cell numbers in the NB lineage. *Mms19* is also required for the growth

109   and assembly of spindle and astral microtubules (MTs). Our results connect these defects to

110   the mis-localization of the microtubule regulator TACC, suggesting that TACC is a downstream

111   target of the mitotic kinase cascade through CAK-Cdk1-Aurora kinases. Additionally, and

112   apparently unrelated to the CAK-Cdk1 axis, we also identified a direct interaction *in vitro*

113   between Mms19 and microtubules and found that Mms19 promotes microtubule stability

114   and bundle formation.

115

4

116 **Results:**

117

118 *Mms19^P* **brains show a microcephaly phenotype**

119 Normal *Drosophila* larvae spend on average 5-7 days at 25°C to pass through the larval stages.

120 In contrast, *Mms19^P* larvae take not only at least 8-10 days to reach the size of outgrown WT

121 third instar larvae, but they also spend a total of around 15 days in the 3rd larval instar stage

122 before they die. These larvae display a typical mitotic phenotype without recognizable

123 imaginal disc tissues (Nag et al, 2018). Even though outgrown *Mms19^P* larvae lack imaginal

124 discs, their brain is still present, although it is much smaller, displaying a microcephaly

125 phenotype (Fig 1A-C). Additionally, the optic lobe (OL) appears deformed or underdeveloped.

126 Compared to the wild type, the total volume of the *Mms19^P* brains and the volumes of the

127 CBs and OLs, too, are drastically reduced (Fig 1E-G). Surprisingly, however, the number of

128 central brain (CB) NBs per brain lobe did not significantly change between the controls and

129 the *Mms19^P* brains (Fig 1D). This implies that the *Mms19^P* NBs have been properly determined

130 and are present, but probably divide slowly, thereby contributing fewer Ganglion Mother

131 Cells (GMCs) and neurons to the CB and resulting in reduced brain size. We expressed wild-

132 type Mms19 fused to eGFP (Mms19::eGFP) under the control of the endogenous *Mms19*

133 promoter in the *Mms19^P* background to test whether the observed phenotype was indeed

134 caused by reduced *Mms19* activity. Mms19::eGFP fully rescued the brain morphology, the

135 volumes of the whole brain lobe as well as the CB and OL sizes (Fig 1A-G). This not only

136 confirmed that the defects observed in the mutant are indeed due to the absence of *Mms19*

137 activity and not due to a second site mutation on this chromosome, it also showed that the

138 Mms19::eGFP fusion protein is functional.

139 A mitotic activity of *Mms19* was described to promote the Cdk-activating kinase activity of

140 the Cdk7/CycH/Mat1 complex (CAK complex; Nag et al, 2018). The responsible mechanism

141 appears to be a competitive binding of Mms19 to Xpd, which would otherwise recruit CAK to

142 TFIIH, where it assumes a different substrate specificity and is unable to activate the M-Cdk

143 Cdk1. The key result that lead to this model was that the lack of imaginal discs caused by the

144 absence of *Mms19* activity could be rescued considerably by expressing the CAK complex

145 components under the control of the Upstream Activating Sequence (UAS) enhancer, using

146 the *daughterless*(*da*)-Gal4 driver in the *Mms19^P* background (da>CAK, *Mms19^P*) (Nag et al,

147 2018). We therefore tested whether it was possible to rescue the small brain phenotype by

148   the identical strategy. This was not the case, as both CBs and OLs remained smaller (Fig 1A-

149   G). In da>CAK, $Mms19^P$ brains, the number of CB NBs was similar as in the wild type (Fig 1D),

150   even though the overall brain volume was reduced. These observations indicated that the

151    $Mms19^P$ CB NBs probably did not proliferate enough to produce the normal amount of

152   neuronal tissue, and that this defect might not only be caused by insufficient CAK activity.

153   This result therefore points to the possibility that Mms19 acts through two different pathways

154   to achieve normal organ size.

155

156   Higher fraction of $Mms19^P$ NBs in mitosis

157   In order to better understand the microcephaly phenotype, we performed 5-Ethynyl-2'-

158   deoxyuridine (EdU) incorporation assays coupled with pH3 staining and examined defects in

159   cell cycle progression in the NBs. Based on pH3 and EdU staining, the cells can be allocated

160   to one of the following phases: only EdU = S, i.e. cells in S phase; pH3 without EdU = M, i.e.

161   cells undergoing mitosis; both EdU and pH3 =G2/M, i.e. cells transiting from S to G2/M phase;

162   and neither EdU nor pH3 (= G1/G0, i.e. Gap phase) (Fig S1A). NBs were marked with

163   antibodies against Miranda (Mira) and the number of cells were counted in each class. The

164   results are represented as a percentage of the total number of cells per brain lobe. We

165   observed that about half the cells were not labelled (i.e. G1/G0 cells: 47-56%; Fig S1B) and

166   the relative differences between the genotypes were small. However, lack of $Mms19$ caused

167   a clear increase in the fraction of cells in M phase (35% compared to 24% in the wild type; Fig

168   S1E). This result could either mean that more cells undergo divisions or that the $Mms19^P$ NBs

169   are either trapped in M phase or proceed more slowly through it.

170   Interestingly, the small class of cells that are EdU$^+$ and pH3$^+$ showed the highest relative

171   increase in frequency when CAK was overexpressed (Fig S1D; 6.5% vs 3.2% for $Mms19^P$).

172   Double positive cells have gone through S phase and were in M-phase at the time of fixation.

173   The fact that overexpression of CAK leads to a higher frequency of double positive cells is

174   consistent with the idea that these cells are progressing through the cell cycle more rapidly

175   and/or that they enter M-phase prematurely.

176

NBs depend on *Mms19* for timely and coordinated spindle assembly and spindle orientation

To study how *Mms19* contributes to spindle assembly and progression through mitosis, we utilized a transgene that expresses EB1::GFP, a MT plus end binding and tracking protein that labels growing MT ends (Zhu et al, 2009). Live imaging of NBs expressing EB1::GFP revealed the dynamics of the formation of the mitotic spindle and allowed us to estimate the duration of mitosis, which we defined as the period from the onset of the Nuclear Envelope Break-Down (NEBD) until the end of cytokinesis. NEBD onset was determined by the appearance of the GFP signal in the nuclear region, which lacks a GFP signal until NEBD. NBs expressing EB1::GFP in the wild-type background finished cytokinesis approximately 10 min after NEBD (Fig 2A, mov 01). On the other hand, NBs expressing EB1::GFP in an $Mms19^P$ background reached cytokinesis only around 20 min after NEBD (Fig 2B, mov 02).

Interestingly, in some of the EB1::GFP expressing $Mms19^P$ NBs, the spindle formation started before the two centrosomes had finished migrating to the opposite sides of the nucleus (Fig 2B, mov 03). As a result, at 3 min, a kinked spindle was observed, which eventually straightened out at 5 mins. Around 10% kinked spindles were found in $Mms19^P$ NBs. In one case of a $Mms19^P$ NB spindle, only one centrosome started nucleating MTs (Fig 2C). The spindle remained monopolar until 6 min post NEBD and only then, a bipolar spindle became apparent. Further, around 20% of the spindles in $Mms19^P$ NBs changed their orientation during the course of mitosis (Fig 2B, B', mov 03), while all wild type spindles examined remained firmly anchored at the cortex and did not change their orientation (Fig 2A, A').

Drosophila larval NBs are characterized by a defined apical-basal polarity (Homem et al, 2012) where the atypical Protein Kinase C (aPKC)-Bazooka-Pins complex localizes to the apical cortex while Miranda localizes to the basal cortex (Fig S4A). As differentiation of the GMC relies on the inheritance of the Mira-bound cargo, the orientation of the mitotic spindle is tightly coupled to this apical basal polarity axis (Schuldt et al, 1998; Rolls et al, 2003). We therefore further examined the spindle orientation defects in fixed cells labelled with the polarity marker Miranda (Mira), which localizes to the basal cortex of the NB, forming a crescent-like pattern. We found that most of the WT spindles form at an angle of 10 degrees or lower relative to Mira. On the other hand, $Mms19^P$ NBs more frequently failed to align their spindles within 10 degrees (Fig S4C-D) and the largest tilt that we observed was around 60°. However, a marked effect on cell fate determination was observed previously only when

209   the spindle angle was close to 90° (Lee et al, 2006; Cabernard and Doe, 2009). In this case

210   spindles oriented at around 90° led to both the daughter cells assuming the NB identity, thus

211   increasing NB numbers per brain lobe. Consistent with this spindle orientation defect being

212   insufficient to cause major NB amplification, we did not see a significant difference in the NB

213   number per brain lobe between wild-type $Mms19^P$ (Fig 1D). Therefore, the spindle orientation

214   defect due to lack of $Mms19$ does not appear to lead to differentiation problems, but impedes

215   efficient mitosis.

216   We conclude that in the absence of $Mms19$, spindle formation is not properly coordinated

217   with cell cycle progression and that defects in centrosome migration and in spindle assembly

218   and orientation contribute to the delay of the mitosis in $Mms19^P$ NBs.

219

220   **$Mms19$ is cell autonomously required to maintain normal cell numbers**

221   In the experiments with the $Mms19^P$ mutants, Mms19 was absent from all larval cells. In this

222   situation, the mitotic delay could be due to a systemic effect or due to the lack of a cell

223   autonomous activity of Mms19. To test whether $Mms19$ is specifically required in the mitotic

224   cells for the timely progression through mitosis, we generated $Mms19^P$ mosaic NB clones in

225   an otherwise wild-type background. Mosaic clones were induced in NBs 24hrs after larval

226   hatching (ALH) and the expansion of these clones was analyzed by dissecting the brains in

227   mid-third instar larvae 72 hrs ALH. For this experiment, we focused on the type I NBs on the

228   ventral side. On average, 45 cells per clone were counted in control clones, but only around

229   30-35 cells in $Mms19^p$ clones ($P<0.05$; Fig S2 A-C), indicating that the loss of $Mms19$ activity

230   hinders the establishment of normal cell numbers in the NB lineage. This observation

231   reaffirms our conclusion that absence of $Mms19$ delays mitosis in NBs and that this mitotic

232   delay probably causes more $Mms19^P$ NBs to linger in M-phase (Fig S1E).

233
234

235   **$Mms19$ is required to form spindles of a normal length and density**

236     $Mms19^P$ spindles are generally shorter than the wild-type ones (Fig 3A-E). In normal NB

237   spindles, the centrosomes were anchored close to the cell cortex, with spindle MTs

238   emanating from them and extending to the chromosomes (Fig 3A, A'). But in around a quarter

239   of the mutant cells, even though the chromosomes were aligned at the metaphase plate, the

240   centrosomes were connected to the cell cortex and were only a short distance away from the

241   metaphase plate (Fig 3B, B'). In order to quantify this defect, we measured the length of the

242   spindles across all genotypes and found that the spindles in $Mms19^P$ and da>CAK, $Mms19^P$

243   were significantly shorter than the wild-type control spindles (Fig 3C). As the NBs were also

244   considerably smaller in $Mms19^P$ and da>CAK, $Mms19^P$ brains (Fig 3D), we additionally

245   displayed the spindle length relative to the cell diameter (Fig 3E). A ratio closer to 1 indicates

246   that the centrosomes were anchored close to the cell cortex, as in a healthy spindle. On the

247   other hand, if the ratio was equal to or lower than 0.6, the spindle was defined as a 'short

248   spindle' because the centrosomes were further inside the cell. We found a significant

249   reduction in this ratio in $Mms19^P$ and da>CAK, $Mms19^P$ NB spindles (Fig 3E). $Mms19^P$ NBs

250   contained around 20% short spindles while this number went up to 30% for da>CAK, $Mms19^P$

251   (Fig 3F). This data indicates that the short spindle phenotype was not rescued, but actually

252   worsened upon overexpression of CAK. On the other hand, expression of Mms19::eGFP in the

253    $Mms19^P$ background rescued the short spindle phenotype and only 3% of the NBs displayed

254   it.

255   To determine the effect of $Mms19$ on MT formation and stability, we measured astral as well

256   as inner spindle MT density. For astral MT quantification, we used the method described by

257   Yang and co-workers (Yang et al, 2014; Fig 3G) and found a significant reduction in the

258    $Mms19^P$ NBs as compared to wild type (Fig 3H-I). This phenotype appeared to be slightly

259   rescued by CAK complex overexpression and was fully rescued by expressing Mms19::eGFP

260   in the $Mms19^P$ background. Reduced astral MT stability could be linked to the spindle

261   positioning and orientation defects described previously (Fig 2B, 2E, S4B-D) as astral MTs

262   were shown to contact the cell cortex and regulate spindle positioning (Pearson et al, 2004).

263    $Mms19$ is thus necessary for the formation of fully assembled spindles and astral MTs.

264

265

266   **$Mms19$ assists MT polymerization *in vivo***

267   To assess whether the short spindles could result from a defect in MT growth *in vivo*, we

268   studied NBs expressing EB1::GFP. Live imaging of EB1::GFP revealed the path of elongation of

269   single MTs, akin to that of a comet, and the movement speed of the GFP signal reflects the

270   growth speed of the MT plus ends. Wild-type and $Mms19^P$ larval brains expressing EB1::GFP

271   were dissected and live imaging was performed. The speed of the EB1::GFP particles was then

272   tracked manually using ImageJ. The measurements indicated that the spindle MTs of wild-

273   type NBs polymerized at a rate that is significantly higher than the rate observed in $Mms19^P$

274   NBs (Fig 4A, A', WT-mov 04, $Mms19^P$ -mov 05). To assess whether the MT assembly function

275   of $Mms19$ is restricted to the mitotic state, we also tested whether the absence of $Mms19$

276   also affects MT polymerization in the post mitotic glia cells. Measuring EB1 comet speeds in

277   glia cells showed a decrease in MT growth for $Mms19^P$ glia as compared to wild-type glia (Fig

278   4B, B', WT-mov 06, $Mms19^P$ -mov 07). These results established that $Mms19$ assists MT

279   polymerization and growth *in vivo* in mitotic NBs and in postmitotic glia.

280   Perhaps due to reduced MT growth, spindle assembly is also delayed in $Mms19^P$ brain NBs.

281   Approximately 3 minutes after the onset of NEBD, a spindle fully assembled in wild-type NBs

282   (Fig 4C). In contrast, in most $Mms19^P$ NBs, 3 minutes after the onset of NEBD the 'spindles'

283   appear to be short and MT density seems much lower than in the wild type (Fig 4D). In the

284   presented case, it took 7 minutes from the start of NEBD until a fully assembled spindle

285   became visible (Fig 4D).

286

287   ***Mms19* is required for spindle re-polymerization**

288   The short spindles observed in $Mms19^P$ NBs might be caused by impaired MT polymerization.

289   To test whether Mms19 modulates MT polymerization dynamics, we utilized the *in vivo* MT

290   polymerization assay described by Gallaud and co-workers (Gallaud et al, 2014). With this

291   procedure, the NB spindles were completely depolymerized after incubation on ice for 30 min

292   (Fig 5A). Wild-type NB spindles then regained their standard size and morphology within 90

293   sec after shifting them back to 25°C (Fig 5A). In $Mms19^P$ NBs, however, the spindles failed to

294   re-polymerize to the normal shape after 90 sec. Instead, they remained abnormally short (Figs

295   5B, 5E). Interestingly, whereas the Mms19::eGFP fusion protein was able to rescue this

296   phenotype, CAK overexpression was unable to do so (Fig 5C-E). To validate this short spindle

297   phenotype, we also calculated the spindle sizes relative to the cell diameter after 90 sec

298   incubation at 25°C (Fig 5F). Even though $Mms19^P$ cells are smaller, their normalized spindle

299   size was still significantly smaller than the wild-type one. When CAK was overexpressed in

300    $Mms19^P$ NBs, the spindle became slightly longer than in $Mms19^P$, but it still remained shorter

301   than in the $Mms19^P$ mutant rescued with the wild-type Mms19::eGFP transgene (Fig 5F). This

302   result shows that $Mms19$ has an important role in promoting spindle polymerization and

303   mainly through a CAK independent process.

304

Centrosomal localization of the MT regulator TACC depends on *Mms19*

306 Transforming Acidic Coiled-Coil (TACC), a downstream target of Aurora A kinase, is a critical

307 regulator of centrosomal MTs. During mitosis, Aurora A phosphorylates TACC and stimulates

308 its localization on the centrosomes, where TACC further recruits mini-spindles (Msps). Loss-

309 of-function mutations in either *Aurora A*, *TACC* or *Msps* show drastic abnormalities in astral

310 and spindle MTs (Giet et al, 2002; Bird and Hyman, 2008). As *Mms19^P* NBs display defects in

311 centrosomal separation, spindle length and astral MTs, we examined whether Aurora A and

312 TACC might be involved in the same process as Mms19 and if the absence of functional

313 *Mms19* impedes *TACC* function. We therefore stained wild-type and *Mms19^P* NBs for TACC

314 and observed a strong signal at the wild-type centrosomes (Fig 6A). On the other hand, in

315 >50% of *Mms19^P* NBs, TACC did not show any enrichment on the centrosomes (Fig 6B, D).

316 Similar results were also obtained with its interactor Msps (Fig S6). As TACC acts downstream

317 of Aurora A kinase, and Aurora itself acts downstream of Cdk1 (Van Horn et al, 2010), this

318 defect might be caused by insufficient CAK activity in *Mms19* mutants (Nag et al, 2018). We

319 therefore tested this hypothesis by over-expressing the three CAK components in the *Mms19^P*

320 background (da>CAK, *Mms19^P*). Indeed, upon CAK overexpression, the fraction of spindles

321 displaying centrosomal TACC almost reached wild-type levels (Fig 6C, D). To quantify the

322 enrichment of TACC on centrosomes, we compared the fluorescent intensity of centrosomal

323 TACC to the TACC fluorescent intensity on the spindle. This ratio decreased for *Mms19^P* NBs,

324 but was rescued in da>CAK, *Mms19^P* NBs (Fig 6E). It was also reported that *Aurora A* loss-of-

325 function can cause centrosome fragmentation (Giet et al, 2002). Co-staining *Mms19^P* NBs with

326 antibodies against the centrosomal protein γ-Tubulin showed that even in cases with

327 apparent TACC mis-localization, centrosomal γ-Tubulin was still present, indicating that TACC

328 mislocalization is not caused by centrosome fragmentation. These findings indicate that

329 centrosomal localization of TACC and its stimulation of astral and spindle MT stability or

330 growth is at least partially dependent on *Mms19* activity.

331

Mms19 binds to MTs and stimulates MT assembly

333 To explore the possibility that Mms19 also functions through different activities, we prepared

334 protein extracts from flies expressing Mms19::eGFP driven by its endogenous promoter (Nag

335 et al, 2018), subjected them to immunoprecipitations and analyzed co-purifying proteins by

336   Mass spectrometry (Supplementary Table S1). Adult wild-type flies and Imp::eGFP expressing

337   flies, respectively, served as controls to exclude any non-specific binding to beads and GFP,

338   respectively. Amongst the proteins exclusively bound to Mms19::eGFP were the CIA proteins

339   Mip18, Ciao1 and Ant2, which form a complex with Mms19 to mediate Fe-S cluster delivery

340   (Gari et al, 2012; Stehling et al, 2012). The fact that we recovered these proteins efficiently,

341   indicated that the purification was efficient. Because *Mms19* functions on microtubules and

342   our second control, IMP::eGFP, is also involved in MT dependent processes, we additionally

343   inspected the data for tubulin and MT binding proteins that are enriched by the Mms19::eGFP

344   compared to the wild-type control without eGFP tag (Supplementary Table S2). This

345   comparison revealed a clear enrichment of tubulin and several Microtubule Associated

346   Proteins (MAPs). Some of the associated proteins were not present at all in the wild-type

347   control, some were present, but at lower levels compared to the Mms19::eGFP and

348   IMP::eGFP fractions. Others were exclusively found in the Mms19::eGFP fraction. These

349   results therefore suggested that Mms19 might directly or indirectly bind to MTs.

350   To validate the interaction of Mms19 with Tubulin, we next tested whether Mms19::5xHis

351   purified from *E. coli* and α/β-tubulin dimers interact *in vitro.* Mms19::5xHis was incubated at

352   an equimolar ratio with purified porcine brain α/β-tubulin and then bound to the Ni-NTA

353   resin. All incubations and washing steps were carried out at 4°C. Copurifying proteins where

354   then assessed by western blotting. A band corresponding to α-tubulin was observed when

355   tubulin was incubated with Mms19::5xHis (Fig 7A, B), but tubulin alone did not bind to the

356   resin, pointing to a direct interaction between tubulin and Mms19::5xHis.

357   To establish whether Mms19 stimulates MT polymerization, assembly or stability, we

358   performed a spectrophotometric assay in which tubulin was incubated with Mms19::5xHis at

359   a 40:1 ratio (Mirigian et al, 2013). The absorbance of this mixture was recorded at 340nm

360   over 40 min. The increase in absorbance of the sample is a measure for the polymerization of

361   MTs. The positive control, a fraction of known MT elongators (Microtubule Associated Protein

362   Rich Fraction (MAPF) produced a similar maximal absorbance (Fig 7C), but this was not seen

363   when either only Mms19 or only tubulin were added (Fig 7C). Furthermore, to distinguish MT

364   polymerization from aggregation, we incubated this mixture after the polymerization at 4°C.

365   If tubulin indeed polymerizes into MTs, this incubation in the cold should de-polymerize the

366   MTs. On the other hand, if the increasing absorbance was due to aggregation of either tubulin

367   or Mms19, the absorbance due to aggregates would not decrease after cold treatment.

368   Because the absorbance of the sample sharply decreased in the cold, we conclude that

369   Mms19 indeed promoted MT polymerization (Fig 7D-D'). Mms19 thus not only binds to

370   tubulin and MTs, it also stimulates MT polymerization, assembly or stability *in vitro.*

371   To better understand the mechanism of modulation of the MT dynamics by Mms19, we

372   complemented the biochemical experiments with a high-resolution optical method.

373   Polymerized MTs were incubated at room temperature (RT) with either BRB80/solvent buffer

374   or with Mms19::5xHis, purified upon expression in *E. coli*. These samples were then visualized

375   by negative-stain electron microscopy (EM). MT fibers in general appeared to be less stable

376   upon addition of BRB80/solvent alone (at RT) as some MT fibers were observed undergoing

377   de-polymerization (Fig 7E) under these conditions. Remarkably, MTs incubated with

378   Mms19::5xHis were comparatively longer (Fig 7F, G) and more bundled (Fig 7H, I).

379   Furthermore, the Mms19::5xHis containing samples contained particles not found in the

380   samples without Mms19 and these particles appeared along the lateral MT surface (Fig 7F,

381   H). It thus appears that Mms19 binds along the surface of MTs, stabilizing MTs and possibly

382   stimulating inter-MT contacts.

383

Discussion:

384
385
386 *Mms19* was initially identified as a gene that regulates the nucleotide excision repair (NER)
387 pathway of DNA repair through its participation in Fe-S cluster assembly. When evidence
388 emerged about a possible NER independent mitotic activity of *Mms19* (Ito et al, 2010; Nag et
389 al, 2018), this warranted further investigation into the precise role of *Mms19* during mitotic
390 spindle assembly in diploid cells. Now we report novel, important roles for *Mms19* during
391 spindle MT assembly and mitotic timing in *Drosophila* NBs. Based on their different
392 suppressibility by elevated CAK levels, *Mms19* phenotypes point to a dual role of the novel
393 mitotic gene *Mms19* in MT assembly. The direct function of Mms19 in binding to, stabilizing
394 and bundling of MTs seems CAK independent and might therefore have an important function
395 in the establishment of other extended microtubule structures, too. Indeed, we found
396 preliminary evidence that this might be the case. Neurites are long projections that emerge
397 in differentiating, postmitotic neurons. They become packed with extended MT bundles
398 which support neurite outgrowth and neuronal signaling. Because these are postmitotc
399 events, this MT formation is not driven by the mitotic kinases. Nevertheless, we found that
400 normal neurite outgrowth depended on Mms19 because *Mms19^P* neuronal cells were unable
401 to extend neurites in *ex vivo* experiments (Fig S8).

402 In mitotic NBs, both Mms19 mechanisms, the CAK independent and the CAK dependent, are
403 required. Nag et al. (2018) had presented a model that explained how Mms19 activates the
404 mitotic CAK and the Cdk1 activity. Their model was based on results with larval imaginal discs.
405 We reaffirmed that this *Mms19* activity is also important in NBs, and we further identified a
406 downstream component of this *Mms19*-CAK-Cdk1 mitotic axis, that seems to mediate this
407 activity, the regulator of centrosomal MTs, TACC. In the CAK dependent pathway model (Fig
408 S3A-B), Mms19 competes with the CAK complex for binding to Xpd (Ito et al, 2010; Nag et al,
409 2018). During mitosis, binding of Mms19 to Xpd prevents the interaction between Xpd and
410 the CAK complex, thus releasing the inhibition of the Cdk-activating kinase activity of CAK by
411 Xpd (Chen et al, 2003; Nag et al, 2018). Our results add an additional dimension to this
412 pathway by linking it to the downstream Aurora A-TACC pathway (Giet et al, 2002; Barros et
413 al, 2005). *Mms19* inactivation prevents normal centrosome localization of TACC and this
414 phenotype is rescued upon expressing additional CAK (Fig 6). Cdk1, the major downstream
415 target of the CAK complex, is known to activate Aurora A kinase during mitosis (Van Horn et

416 al, 2010) and phosphorylation of TACC by Aurora A triggers its centrosomal localization (Giet
417 et al, 2002). Given that the failure of TACC localization in the absence of *Mms19* can be
418 rescued by CAK over-expression, we now propose TACC as a downstream target of the
419 Mms19-CAK-Cdk1 axis and modulation of CAK activity seems to be the main mode of action
420 of Mms19 towards TACC. The best characterized function of TACC is its interaction with Msps
421 which leads to stabilization of astral MTs (Lee et al, 2001). This activity involves their
422 recruitment to the centrosomes, and we found that not only the centrosomal localization of
423 TACC (Fig 6), but also the one of Msps depends on *Mms19* and elevated CAK activity (Fig S6).
424 The activity of *Mms19* through this pathway, which involves the activation of the M-phase
425 regulator Cdk1, therefore contributes significantly to the coordination of cell cycle
426 progression and spindle formation, a process that is affected in the absence of *Mms19* (Fig
427 2).

428 Loss of centrosomal TACC or Msps leads to destabilization of centrosomal MTs and defects in
429 chromosome segregation (Gergely et al, 2000; Lee et al, 2001), indicating that the activity of
430 *Mms19* through this pathway makes an important contribution to MT stability and
431 chromosomal segregation. Interestingly, whereas TACC itself may not directly regulate MT
432 assembly, there is good evidence that its partner Msps, which also requires *Mms19* function
433 to localize to centrosomes (Fig S6), can promote MT polymerization. The *Xenopus* homologue
434 of Msps, XMAP215, and the mammalian homolog, chTOG, have been demonstrated to be
435 processive MT polymerases (Brouhard et al, 2008; Gutierrez-Caballero et al, 2015).

436 CAK overexpression rescued TACC localization, but it could not fully rescue the short
437 spindle/spindle assembly and the microcephaly defects (Figures 1, 3, 5). Furthermore, even if
438 we did not test this directly, we can expect the glial cell MT growth defects (Fig 4B) and the
439 neurite outgrowth defect (Fig S8) to be also independent of the CAK activity because this
440 kinase is mostly active during the mitotic phase of the cell cycle. We found that Mms19
441 interacts directly with tubulin and MTs. This is interesting because previous work had also
442 suggested an interaction with the mitotic spindle (Ito et al, 2010, van Wietmarschen et al,
443 2012, Nag et al, 2018). In this study, we report for the first time a direct interaction between
444 Mms19 and tubulin, and we linked this interaction to an activity of Mms19 in stimulating MT
445 assembly (Fig 7). The EM data indicates that Mms19 might contribute to the assembly of MTs
446 by directly binding to them, bundling them and regulating thereby the stability of MTs.

447   Interestingly, such a MT bundling activity seems also crucial for neurite outgrowth, because

448   the initial stage of this process involves bundling of MTs (Miller and Suter, 2018). This would

449   explain why this process is delayed or blocked in most $Mms19^P$ neurons (Fig S8).

450   Recently, another connection between Fe-S cluster proteins and mitosis was described to

451   involve Kif4a in HEK293 cells (Ben-Shimon et al, 2018). However, its *Drosophila* homologue,

452   Klp3a, was not amongst the proteins co-purifying with Mms19::eGFP in extracts from adult

453   flies (Table S1) and the *Klp3a* phenotypes described by (Williams et al, 1995) are distinctly

454   different from the ones we found for $Mms19^P$. Nevertheless, it would be interesting to find

455   out whether and where *Mms19* has yet another mitotic function in a metazoan through

456   delivering an Fe-S cluster to Klp3a/Kif4a.

457   Ito and co-workers first proposed the novel 'MMXD' mitotic complex consisting of Mms19,

458   Mip18 and Xpd, that localizes to the mitotic spindle and is required for proper chromosome

459   segregation in human cells (Ito et al, 2010). Interestingly, the epithelial-cell polarity regulator

460   protein Crumbs (Crb) was also shown to form a complex called 'CGX' with Xpd and the

461   *Drosophila* homolog of Mip18, Galla-2 (Yeom et al, 2014). Yeom and colleagues found that

462   Crb and Galla-2 associated with the mitotic spindle and were required for spindle assembly

463   and chromosome segregation in young *Drosophila* embryos and that this function could be

464   connected with the modulation of CAK activity by Xpd (Li et al, 2010). Further, a tissue

465   overgrowth phenotype induced by Crb overexpression was rescued by downregulation of Xpd

466   and/or Galla-2. However, the authors did not describe a Crb-Mms19 interaction and Crb did

467   not appear as a Mms19-interacting protein in our Mass-spectrometry screen. Nevertheless,

468   as Mms19 interacts with both Xpd and Galla-2 (Nag et al, 2018), it seems likely that it could

469   be a part of the mitotic 'CGX' complex. It would thus be interesting to test whether *Mms19*

470   knockdown can also rescue the defects induced by Crb overexpression. Additionally, because

471   neither of the 'CGX' proteins are known to have tubulin binding properties, the possibility

472   exists that Mms19 might recruit the CGX/MMXD proteins to the spindles and co-ordinate

473   spindle assembly and chromosome segregation with them.

474   Multiple MT associated proteins co-operate for the assembly and dynamics of the mitotic

475   spindle. Our *in vitro* studies with *E.coli* expressed Mms19 strongly suggest that Mms19

476   directly interacts with MTs and that this interaction supports MT growth and bundling. It is

477   possible that *in vivo*, interaction of Mms19 with additional factors might then boost this

478 activity. Correspondingly, in the Mass Spectrometry analysis (Supplementary table 1) we also

479 see MT associated proteins such as Lis-1, Kinesin heavy and light chains. Lis-1 is already known

480 to function during spindle assembly and positioning (Moon et al, 2014). The

481 immunopurification of Mms19 and associated proteins was carried out with extracts from

482 total adult flies, where mitotic cells and particularly cells in M-phase are rare. It is therefore

483 possible that our screen for interactions with Mms19 identified primarily proteins that

484 interact in interphase and that we missed M-phase-specific interactions. Such candidates

485 could be members of the kinesin family, like Kinesin-14 and Kinesin-5, that play important

486 roles during mitosis. For instance, Kinesin-5 drives bipolar spindle assembly by cross-linking

487 and sliding anti-parallel MTs and may also have an additional MT polymerase activity (Fink et

488 al, 2007; Ferenz et al, 2010; Chen and Hancock, 2015; Leary et al. 2019). There is thus an

489 exciting possibility that Mms19 may also bind to other spindle specific MAPs and through its

490 MT modulatory activity serve to assist the function of such MAPs. Further evidence in this

491 direction would reveal invaluable aspects about a possible cross-talk between Mms19 and

492 MAPs.

493 It was shown recently that MMS19 protein levels are regulated by ubiquitination and

494 subsequent proteasomal degradation in human cells by the ubiquitin ligase MAGE-F1 (Weon

495 et al, 2018). Weon and colleagues showed that the human MMS19 is ubiquitinated at the C-

496 terminal Lysine 993. Alignment of the human and *Drosophila* Mms19 sequences revealed

497 that the human Lys 993 is conserved in *Drosophila* and, additionally, the PTM code 2 software

498 identified this region in *Drosophila* Mms19 as a potential ubiquitinylation site (Minguez et al,

499 2012, Fig S7). This regulatory mechanism also links MMS19 to certain cancers, especially lung

500 squamous cell carcinomas, where MAGE-F1 was found to be upregulated (Weon et al, 2018).

501 In these tumor cells, up-regulation of MAGE-F1 correlated with increased mutational load and

502 the authors connected these mutations to compromised DNA repair that might lead to

503 chromosomal instability (CIN) due to excessive degradation of MMS19 by MAGE-F1. In

504 support of this view, knock-down of MAGE-F1 considerably slowed tumor growth in a mouse

505 xenograft model. But results from our study as well as previous reports (Ito et al, 2010; Nag

506 et al, 2018) provide strong evidence for the roles of Mms19 in MT assembly and spindle

507 formation and its misfunction in this process could cause CIN, leading to the mutational

508 burden. The mitotic defects we observed upon loss of functional *Mms19* did not lead to high

509 levels of aneuploidy in otherwise healthy NBs (Fig S5). However, in rapidly dividing tumor cells

510 carrying oncogenic driver mutations (and lacking tumor suppressor or mitotic checkpoint

511 functions), spindle defects caused by loss of *MMS19* function could possibly amplify the DNA

512 damage effects and CIN. Indeed, high levels of aneuploidy were observed in human HCT116

513 cell lines and in *Drosophila* syncytial embryos with reduced *Mms19* function (Ito et al, 2010;

514 Nag et al, 2018). Our results, therefore, provide support for the interpretation that this novel

515 spindle assembly function of *Mms19* might play an important role in preventing CIN and

516 tumor formation in rapidly dividing cells.

517 Our findings have uncovered novel insights about the mechanism of spindle assembly by

518 *Mms19.* Moreover, as these activities involve a direct association of Mms19 with either Xpd

519 or MTs, the functions described here are most likely independent of the NER role of Mms19.

520 We have also found evidence for a possibly non-mitotic MT regulatory role of *Mms19* for

521 neurite outgrowth. It will be interesting to further analyze the function of Mms19 during the

522 various stages of neurite outgrowth and how its expression and localization is regulated in

523 neurons. A gene that was initially described as a NER regulator, *Mms19* now has the additional

524 roles as a mitotic gene and a MT regulator assigned to it. For the critical roles it fulfils, the

525 proper control of Mms19 expression and localization must be crucial, and erroneous

526 activation of CAK or MT assembly are likely to lead to defects in cell cycle progression. Future

527 studies should therefore address the transcriptional and post-translational control of Mms19

528 expression and localization and how this impacts its functions in cell physiology, development

529 and diseases.

530

Materials and Methods

Key resources tables

The following table lists the fly stocks used in this study:

Fly stocks		
Reagent	**Description**	**Source**
P{*EPgy2*}*Mms19EY00797*/TM3, Sb1 Ser1 (*Mms19^P*)	P-element insertion in the third exon of *Mms19*	Bloomington stock center #15477
+; *Mms19::eGFP, Mms19^P*	eGFP-tagged Mms19 protein expressed in *Mms19^P* background	own work (Nag et al, 2018)
+; *EB1::GFP/CyO*	GFP-tagged EB1 protein expressed under the poly-ubiquitin promoter	provided by Regis Giet
+;*EB1::GFP/CyO; Mms19^P/Tm6,Tb*	EB1::GFP expressed in the *Mms19^P* background	generated in this study
hs-flp/hs-flp; tub-Gal4, UAS-mCD8::GFP/CyO, actin::GFP; FRT82B, tub-Gal80/TM6, Tb	MARCM driver stock	provided by Bruno Bello
+; *FRT82B, Mms19^P/TM6, Tb*	*FRT82B* recombined with *Mms19^P*	own work (Nag et al, 2018)
da-Gal4/CyO, mCherry; UAST-Mat1, Mms19^P/TM3, Ser, GFP	Stock for overexpression of CAK in the *Mms19^P* background	own work (Nag et al, 2018)
UAST-Cdk7/CyO, mCherry/ UAST-CyclinH, Mms19^P/TM3, Ser, GFP	Stock for overexpression of CAK in the *Mms19^P* background	own work (Nag et al, 2018)

538 **The following table lists the primary and secondary antibodies used for immunostainings:**

Primary antibodies			
Antibody	**Manufacturer**	**Catalog number**	**Dilution**
Rat anti-Miranda	Abcam	Ab197788	1:250
Rabbit anti-alpha Tubulin	Abcam	Ab18251	1:500
Mouse anti-alpha Tubulin	Sigma	T6199	1:500
Rabbit anti-GFP	Immunokontakt	210-PS-1GFP	1:500
Rabbit anti-pH3	Cell Signaling	9701	1:200
Rabbit anti-Mms19	Genscript	Custom antibody	1:500
Mouse anti-γH2av	DSHB	UNC93-5.2.1	1:20
Rabbit anti-PKC ζ (aPKC)	Santa-Cruz Biotechnology	sc-216	1:2,000
Mouse anti-Futsch	DSHB	22C10	1:20
Mouse anti-γTubulin	Sigma	T6557	1:1,000
Rabbit anti-TACC	provided by Jordan Raff	-	1:1,000
Rat anti-Elav	DSHB	7E8A10	1:20
Rabbit anti-Msps	Provided by Hiro Ohkura	-	1:1,000
Secondary antibodies			
Goat anti-rat Cy3	Jackson Immuno	112-165-167	1:150
Goat anti-mouse Alexa 488	Invitrogen	R37120	1:500
Goat anti-rabbit Alexa 488	Invitrogen	A27034	1:500
Goat anti-mouse Alexa 647	Invitrogen	A21235	1:500

539

20

540 **The following table lists the antibodies used for probing western blots:**

Primary antibodies			
Antibody	Manufacturer	Catalog number	Dilution
Rabbit anti-Mms19	Synthesized by Genscript Inc.	Custom antibody	1:2,000
Rabbit anti-alpha Tubulin	Abcam	Ab18251	1:2,000
Secondary antibodies			
Goat anti-rabbit HRP	Thermo Fischer Scientific	65-6120	1:10,000

541

542 **Following table lists the kits and reagents used in this study:**

Reagent/Kit	Manufacturer	Catalog number
Aqua Poly/Mount mounting medium	Polysciences Inc	18606-20
Click-it EdU incorporation kit, Alexa Flour 647	Thermo Fischer Scientific	C10340
Paclitaxel (Taxol)	Sigma	T7402
Purified porcine Tubulin	Cytoskeleton Inc	T240-B
MAPF (MT associated protein rich fraction from bovine brain)	Cyoskeleton Inc	MAPF-A
Schneider's Drosophila medium	ThermoFischer Scientific	21720-024
Hoechst 33342	ThermoFischer Scientific	H3570
Protein G Mag Sepharose Xtra	GE life sciences	28967066
Ni-NTA agarose	Qiagen	30210
Collagenase I	Sigma-Aldrich	C0130-100MG
Phenylmethylsulfonyl fluoride (PMSF)	Sigma-Aldrich	10837091001
cOmplete™, Mini, EDTA-free Protease Inhibitor Cocktail	Sigma-Aldrich	4693159001

Concanavalin A	Sigma-Aldrich	C7898
Formamide	Sigma-Aldrich	F9037-100ml
Uranyl acetate	Electron microscopy sciences	22400
1,4-Piperazinediethanesulfonic acid, Piperazine-1,4-bis(2-ethanesulfonic acid), Piperazine-N,N'-bis(2-ethanesulfonic acid) (PIPES)	Sigma-Aldrich	P6757
5' Cy5 labeled Oligonucleotide probe: 5' Cy5-AACACAACACAACACAACACAACACAACACAACAC	Microsynth AG	ChrII
Aphidicolin	Sigma-ALdrich	A0781
Software		
Software	**Source**	**Version**
Fiji (ImageJ)	https://imagej.net/Fiji	-
Leica Application Suite (LAS X)	Leica microsystems	-
PRISM	Graph pad software	Version 5

543

Method Details

545

Dissection and immunostaining of larval brains

547 Larval brains were dissected and stained as described (Daul et al, 2010). Briefly, wandering

548 third instar larvae were dissected in PBS and fixed for 15min in 4% paraformaldehyde

549 supplemented with 5mM MgCl$_2$ and 1mM EGTA (to stabilize MTs). After 3 washes in

550 PBS+0.1% TritonX-100 (PBST), primary antibodies were added. After overnight incubation, the

551 brains were washed 3x with PBST, stained with secondary antibodies and mounted on glass

552 slides in Aqua Polymount mounting medium (Polysciences).

553 For MT regrowth assays, brains were dissected in Schneider's medium (supplemented with

554 10% fetal bovine serum) at 25°C and incubated on ice for 30 min to depolymerize MTs. Brains

555 were then incubated for different time points in a 25°C water bath, followed by fixation and

556 immunostaining. This experiment was performed three times and 20 spindles were analyzed

557 in each iteration. Slides were imaged on a Leica TCS-SP8 microscope (Leica Microsystems)

558   equipped with a 63X, NA 1.4 Plan Apochromat objective. Images were acquired using LAS X

559   software and analyzed using Fiji/ImageJ (Schindelin et al., 2012).

560

561   **Measuring brain compartment volumes**

562   Whole brain lobes were immunostained with antibodies against Miranda (Mira) and

563   phospho-Histone 3 (pH3), and DNA was visualized with Hoechst 33342. Z stacks were acquired

564   with a TCS-SP8 confocal microscope on a 63X, 1.4NA Plan-Apochromat objective with 1µm

565   spacing between each optical section. Segmentation, volume measurement and 3D

566   reconstruction was performed by using the TrackEM2 plugin in Fiji (Cardona et al, 2012).

567

568   **MARCM crosses**

569   For generating mosaic clones the driver stock *hs-flp; tub-Gal4, UAS-mCD8::GFP/CyO,*

570   *actin::GFP; FRT82B, tub-Gal80/TM6*, Tb was crossed to *+; FRT82B, Mms19^P/TM6, Tb.* GFP-

571   Balancer negative 24hr old larvae were selected and heat shocked at 37°C in a glass vial

572   submerged in a water bath for 15min. Larvae were then returned to 25°C and the brains of

573   the non-Tubby larvae were dissected 48hrs later.

574

575   **Live imaging**

576   Brains expressing EB1::GFP were dissected and mounted on stainless steel chambers as

577   described in (Cabernard et al, 2013). Brains were then imaged using a 100X, NA 1.3 oil

578   immersion objective on a Visiscope Spinning disk microscope (Visitron GmbH) fitted with

579   Nikon Ni2 stand and a Photometrics Evolve 512 EMCCD camera. Images were acquired for 60

580   seconds at of 500ms time intervals at 200ms exposure at 60% laser power (488nm). To track

581   the particle velocities, the particles were manually traced in Fiji/ImageJ (Schindelin et al.,

582   2012). Probably due to limited resolution, it was not possible to unambiguously account for

583   merging or splitting events and therefore only particles with a linear trajectory, which did

584   neither split nor merge, were analyzed. At least 5 particles from each spindle were analyzed

585   from a total of 11 cells per genotype. For surface glia quantification, at least 10 particles were

586   analyzed from each of the 15 brains. Stacks were exported to .AVI movies at 14 frames per

587   second.

588

589 To measure the duration of mitosis, EB1::GFP expressing brains were mounted as described
590 above and imaged at 40% laser power with a 63X, 1.3 NA objective of a Nikon W1 LIPSI
591 spinning disk microscope fitted with a Photometrics Prime 95B CMOS camera. Movies were
592 acquired on Nikon's NIS elements software for 2hrs with an interval of 1 min at 200 ms
593 exposure. Z-stacks were acquired simultaneously with 2µm distance between successive
594 optical sections. Movies were analyzed and processed with Fiji/ImageJ. Stacks were exported
595 to .AVI movies at 12 frames per second.

596

597 **Quantification of spindle orientation:**

598 The orientation of the mitotic spindle was examined with respect to the basal Mira crescent.
599 A reference line was drawn passing approximately through the center of the Mira crescent
600 and the angle between the spindle and this reference line was determined using the ImageJ
601 angle tool.

602

603 **EdU incorporation**

604 Click-it EdU kit (Invitrogen) was used to measure EdU incorporation. Brains were dissected in
605 PBS and incubated in Schneider's medium supplemented with 10µM 5-Ethynyl-2'-
606 deoxyuridine (EdU) for 2hrs at 25°C. EdU is an analogue of Thymidine and is incorporated by
607 S phase cells during DNA replication. EdU is then detected due to its binding to a dye-azide
608 conjugate. Brains were subsequently fixed with 4% PFA and incubated with primary
609 antibodies (anti-Mira to mark NBs and anti-pH3 to mark mitotic cells) and secondary
610 antibodies. Subsequently, they were processed for EdU detection following the manufacturer
611 instructions.

612

613 **Preparation of whole-fly extract**

614 1g of flies were collected in Eppendorf tubes and frozen in liquid nitrogen. Frozen flies were
615 crushed into a fine powder using a pre-cooled mortar pestle. The powder was incubated in
616 lysis buffer (25mM Hepes, 150mM NaCl, 1mM EDTA, 0.1% TritonX-100, 1mM
617 phenylmethylsulfonyl fluoride (PMSF), 1 complete EDTA-free protease inhibitor tablet
618 (Roche/Sigma-Aldrich)) for 30 min and then centrifuged in an Eppendorf tube for 30 min at
619 16,000 g and 4°C. The supernatant was saved and snap frozen in liquid nitrogen.

620

Immunoprecipitation to prepare extract for Mass Spectrometry

ProteinG-Mag Sepharose (GE) beads were washed 3X with PBS, incubated for 2hrs with anti-GFP antibody. Beads were then incubated with the crude extracts for 6hrs at 4°C. Following 3 washes with the wash buffer (25mM Hepes, 150mM Nacl, 1mM EDTA, 1mM PMSF, 1 tablet complete EDTA free protease inhibitor tablet), bound proteins were eluted by 15 min incubation in urea elution buffer (6–8 M Urea, 20 mM Tris pH 7.5, and 100 mM NaCl) or glycine elution buffer (100mM Glycine, pH 2.6. These eluates were neutralized by adding 150mM Tris-Cl, p 8.8).

Mass-Spectrometry

Eluted proteins in 8M urea were processed essentially as described by Engel and colleagues (Engel et al, 2014). Briefly, proteins were reduced by addition of 1/10 volume of 0.1 M DTT and incubated for 30 min at 37°C, followed by alkylation with a five-fold molar excess of iodoacetamide and incubation for 30 min at 37°C. Proteins were precipitated at -20°C by addition of 5 volumes cold acetone and incubation for 30 min at -20°C. All liquid was carefully removed, and the pellet dried in ambient air for 15 min before reconstitution of the proteins in 8 M urea, 50 mM Tris-HCl pH 8.0 to a final protein concentration between 0.2-0.3 mg/mL. Protein concentration was determined by Bradford assay. An aliquot corresponding to 5 μg protein was diluted to a final urea concentration of 2 M urea with 20 mM Tris-HCl pH 8.0, and 2 mM CaCl2. Proteins were digested by trypsin (1:50 (w/w) trypsin/protein ratio) for 6 hours at 37°C. The digests were acidified with TFA (1%) and analyzed by LC-MS/MS (EASY-nLC 1000 coupled to a QExactive HF mass spectrometer, ThermoFisher Scientific) with three repetitions injecting an aliquot of 500 ng protein. Peptides were trapped on an Acclaim PepMap100 C18 pre-column (3μm, 100 Å, 75μm x 2 cm, ThermoFisher Scientific, Reinach, Switzerland) and separated by backflush on a C18 column (3μm, 100 Å, 75μm x 15 cm, Nikkyo Technos, Tokyo, Japan) by applying a 40 min gradient of 5% acetonitrile to 40% in water, 0.1% formic acid, at a flow rate of 300 nl/min. Peptides of m/z 400-1400 were detected at a resolution of 60,000 m/z 250 with an automatic gain control (AGC) target of 1E06 and maximum ion injection time of 50 ms. A top fifteen data dependent method for precursor ion fragmentation was applied with the following settings: resolution 15,000, AGC of 1E05, maximum ion time of 110 ms, charge inclusion of 2+ to 7+ ions, peptide match on, and dynamic exclusion for 20 sec, respectively.

653 Fragment spectra data were converted to mgf with ProteomeDiscoverer 2.0 and peptide

654 identification made with EasyProt software searching against the forward and reversed

655 UniprotKB *Drosophila melanogaster* protein database (Release 2016_11), complemented

656 with commonly found protein sequences of contaminating proteins, with the following

657 parameters: parent mass error tolerance of 10 p.p.m., trypsin cleavage mode with three

658 missed cleavages, static carbamidomethylation on Cys, variable oxidation on Met and

659 acetylation on protein N-terminus. On the basis of reversed database peptide spectrum

660 matches, a 1% false discovery rate was set for acceptance of target database matches, and

661 only proteins with at least two different peptide sequences identified were allowed.

662

663 **Immunoprecipitation/Pull-down assays**

664 50μg of purified Mms19 (Tagged with 5X Histidine at C-terminus, synthesized by Genscript

665 Inc and solubilized in 20mM Tris, 150mM NaCl, 0.5 M Arginine) was incubated with 50μg

666 purified porcine tubulin (Purchased from Cytoskeleton Inc) at 4°C for 2 hrs. This mixture was

667 subsequently incubated with Ni-NTA agarose (equilibrated with 20mM Tris-Cl and 250mM

668 NaCl) for 1 hr at 4°C. The beads were then washed three times with wash buffer containing

669 20mM Tris, 250mM NaCl and 20mM Imidazole and the bound proteins were eluted by adding

670 elution buffer (20mM Tris, 250mM NaCl and 500mM Imidazole) to the resin on ice for 10 min.

671 The eluate was then analyzed by probing Western blots with anti-Mms19 antibodies and

672 rabbit anti-alpha tubulin antibodies.

673

674 *In vitro* **MT turbidity assay**

675 40μM solution of tubulin (porcine brain, Cytoskeleton, Inc) was prepared in Brinkley's buffer

676 (BRB80, which contains 80mM PIPES buffer, 1mM EGTA, 2mM $MgCl_2$) +10% glycerol and

677 supplemented with 1mM GTP. The tubulin solution was then incubated with test proteins

678 (MAPF 1mg/ml, Mms19 0.16mg/ml (concentration of Mms19 used was 1μM)) at 37°C and

679 absorbance was measured at 340nm on a SpectraMax 340PC microplate reader (Molecular

680 devices). Two negative controls were used: Mms19 only and Tubulin incubated with the

681 solvent in which Mms19 is solubilized (20mM Tris-CL, 150mM NaCl, 0.5M Arginine). Results

682 were validated from four independent experiments.

683

684 **Neuronal *in vitro* cultures**

685 Dissociated brain cells were cultured *in vitro* according to a protocol previously described

686 (Egger et al, 2013). Briefly, 15-20 third instar larvae were dissected in PBS, and washed 3 times

687 with Rinaldini solution (800 mg NaCl, 20 mg KCl, 5 mg NaH$_2$PO$_4$, 100 mg NaHCO$_3$, 100 mg

688 glucose, in 100 ml distilled water). The brains were then incubated in 0.5% collagenase I in

689 Rinaldini solution for 60 min and subsequently washed 4 times in Schneider's medium. The

690 treated tissues were then dissociated by pipetting 100-200 times. The resulting cell mixture

691 was passed through a 40μm mesh to remove cell clusters, and the brain cells were then

692 incubated for 24hrs at 25°C. After 24hrs incubation, the cells were plated on concanavalin A-

693 coated coverslips, fixed and stained.

694

695 **Preparation of MTs for EM**

696 To obtain polymerized MTs, 20μM tubulin was incubated in the presence of 10μM taxol at

697 37°C for 30min. The sample was then subjected to ultra-centrifugation for 10min at 100,000

698 g at 4°C in a Beckman Airfuge ultracentrifuge. The supernatant containing un-polymerized

699 dimers was then removed and the pellet was reconstituted with either 15μl BRB80/solvent

700 (BRB80 components: 80mM PIPES buffer, 1mM EGTA, 2mM MgCl$_2$ + Mms19 solvent

701 constituents: 20mM Tris-CL, 150mM NaCl, 0.5M Arginine) or 15 μl of 0.5μM Mms19::5xHis

702 in BRB80/solvent.

703

704 **Negative stain EM**

705 5 μl of samples were applied on glow discharged, carbon-coated copper EM grids for 1min.

706 The excess sample was then washed off by dipping the grid in milli-Q water. The sample on

707 the grid was then fixed/negatively stained with 2% Uranyl acetate for 30 sec and then the

708 excess fluid was removed by using filter paper. The samples were imaged at a nominal

709 magnification of 63,000x or 87,000x on a FEI Tecnai Spirit EM operated at 80eV and fitted

710 with a digital camera. MT length and number of MT bundles were quantified from images

711 obtained from three independent experiments.

712

713 **Fluorescent *in situ* hybridization (FISH)**

714 The protocol for FISH was adapted from Dernburg, 2011 with minor modifications. Briefly,

715 third instar larval brains were dissected in PBS and fixed with 4% PFA. The brains were then

716 washed 3 times for 10min each with 2xSSCT (0.3M Sodium Chloride, 0.03M Sodium Citrate

717 and 0.1% Tween 20) followed by 10min washes respectively with 2xSSCT/20% Formamide,

718 2xSSCT/40% Formamide, 2xSSCT/50% Formamide. 100ng of the oligonucleotide probe: 5'

719 Cy5-AACACAACACAACACAACACAACACAACACAACAC that binds to a specific region on the 2nd

720 chromosome (Dernburg, 2011) was then added to the Hybridization buffer (20% dextran

721 sulfate, 2xSSCT, 50% Formamide) and this solution was incubated with the brains in a PCR

722 tube. The probes were then denatured at 92°C for 3 min and then allowed to anneal with the

723 chromosomal DNA overnight at 37°C. The sample was then washed thrice at 37°C with the

724 following solutions for 20min each: 2xSSCT/50% Formamide, 2xSSCT/40% Formamide,

725 2xSSCT/20% Formamide. After two more washes with 2xSSCT, the sample was stained with

726 Hoechst, mounted using Aqua-poly mount, and imaged on a Leica SP8 confocal microscope

727 with a 63x objective.

728

729 **Statistical analysis**

730 Data was analyzed using Graph Pad prism 5.0 software. Means of two groups were compared

731 and significance calculated by using unpaired students t-test. Multiple groups were

732 compared, and significance calculated using the Kruskal-Wallis test and the Dunn's post-test.

733

734

735 # Acknowledgments

736

745

References:

Barros, T. P., Kinoshita, K., Hyman, A. A., & Raff, J. W. (2005). Aurora A activates D-TACC-Msps complexes exclusively at centrosomes to stabilize centrosomal microtubules. Journal of Cell Biology. https://doi.org/10.1083/jcb.200504097

Ben-Shimon, L., Paul, V. D., David-Kadoch, G., Volpe, M., Stümpfig, M., Bill, E., … Ben-Aroya, S. (2018). Fe-S cluster coordination of the chromokinesin KIF4A alters its subcellular localization during mitosis. Journal of Cell Science. https://doi.org/10.1242/jcs.211433

Bird, A. W., & Hyman, A. A. (2008). Building a spindle of the correct length in human cells requires the interaction between TPX2 and Aurora A. Journal of Cell Biology. https://doi.org/10.1083/jcb.200802005

Brouhard, G. J., Stear, J. H., Noetzel, T. L., Al-Bassam, J., Kinoshita, K., Harrison, S. C., … Hyman, A. A. (2008). XMAP215 Is a Processive Microtubule Polymerase. Cell. https://doi.org/10.1016/j.cell.2007.11.043

Brugg, B., Reddy, D., & Matus, A. (1993). Attenuation of microtubule-associated protein 1B expression by antisense oligodeoxynucleotides inhibits initiation of neurite outgrowth. Neuroscience. https://doi.org/10.1016/0306-4522(93)90401-Z

Cabernard, C., & Doe, C. Q. (2013). Live imaging of neuroblast lineages within intact larval brains in Drosophila. *Cold Spring Harbor Protocols*, *2013*(10), 970–977. https://doi.org/10.1101/pdb.prot078162

Cabernard, C., & Doe, C. Q. (2009). Apical/Basal Spindle Orientation Is Required for Neuroblast Homeostasis and Neuronal Differentiation in Drosophila. *Developmental Cell*. https://doi.org/10.1016/j.devcel.2009.06.009

Cameroni, E., Stettler, K., & Suter, B. (2010). On the traces of XPD: Cell cycle matters - untangling the genotype-phenotype relationship of XPD mutations. Cell Division, Vol. 5. https://doi.org/10.1186/1747-1028-5-24

Cardona, A., Saalfeld, S., Schindelin, J., Arganda-Carreras, I., Preibisch, S., Longair, M., … Douglas, R. J. (2012). TrakEM2 software for neural circuit reconstruction. PLoS ONE. https://doi.org/10.1371/journal.pone.0038011

Chen, Y., & Hancock, W. O. (2015). Kinesin-5 is a microtubule polymerase. *Nature Communications*. https://doi.org/10.1038/ncomms9160

Chen, J., Larochelle, S., Li, X., & Suter, B. (2003). Xpd/Ercc2 regulates CAK activity and mitotic progression. Nature, (424), 228–232.

Daul, A. L., Komori, H., & Lee, C. Y. (2010). Immunofluorescent staining of Drosophila larval brain tissue. Cold Spring Harbor Protocols, 5(7). https://doi.org/10.1101/pdb.prot5460

Dernburg, A. F. (2011). In situ hybridization to somatic chromosomes in drosophila. Cold Spring Harbor Protocols. https://doi.org/10.1101/pdb.top065540

Egger, B., Van Giesen, L., Moraru, M., & Sprecher, S. G. (2013). In vitro imaging of primary neural cell culture from Drosophila. Nature Protocols. https://doi.org/10.1038/nprot.2013.052

Engel, H., Mika, M., Denapaite, D., Hakenbeck, R., Muḧlemann, K., Heller, M., … Hilty, M. (2014). A low-affinity penicillin-binding protein 2x variant is required for heteroresistance in Streptococcus pneumoniae. Antimicrobial Agents and Chemotherapy. https://doi.org/10.1128/AAC.02547-14

Fink, G., Hajdo, L., Skowronek, K. J., Reuther, C., Kasprzak, A. A., & Diez, S. (2009). The mitotic kinesin-14 Ncd drives directional microtubule-microtubule sliding. *Nature Cell Biology*. https://doi.org/10.1038/ncb1877

Ferenz, N. P., Gable, A., & Wadsworth, P. (2010). Mitotic functions of kinesin-5. *Seminars in Cell and Developmental Biology*. https://doi.org/10.1016/j.semcdb.2010.01.019

Gallaud, E., Caous, R., Pascal, A., Bazile, F., Gagné, J. P., Huet, S., … Giet, R. (2014). Ensconsin/map7 promotes microtubule growth and centrosome separation in Drosophila neural stem cells. Journal of Cell Biology, 204(7), 1111–1121. https://doi.org/10.1083/jcb.201311094

Gari, K., Ortiz, A. M. L., Borel, V., Flynn, H., Skehel, J. M., & Boulton, S. J. (2012). MMS19 links cytoplasmic iron-sulfur cluster assembly to DNA metabolism. Science. https://doi.org/10.1126/science.1219664

Gergely, F., Kidd, D., Jeffers, K., Wakefield, J. G., & Raff, J. W. (2000). D-TACC: A novel centrosomal protein required for normal spindle function in the early Drosophila embryo. *EMBO Journal*. https://doi.org/10.1093/emboj/19.2.241

Giet, R., McLean, D., Descamps, S., Lee, M. J., Raff, J. W., Prigent, C., & Glover, D. M. (2002). Drosophila Aurora A kinase is required to localize D-TACC to centrosomes and to regulate astral microtubules. Journal of Cell Biology. https://doi.org/10.1083/jcb.200108135

Gutiérrez-Caballero, C., Burgess, S. G., Bayliss, R., & Royle, S. J. (2015). TACC3-ch-TOG track the growing tips of microtubules independently of clathrin and Aurora-A phosphorylation. Biology Open. https://doi.org/10.1242/bio.201410843

Homem, C. C. F., & Knoblich, J. A. (2012). Drosophila neuroblasts: a model for stem cell biology. Development, 139(23), 4297–4310. https://doi.org/10.1242/dev.080515

Ito, S., Tan, L. J., Andoh, D., Narita, T., Seki, M., Hirano, Y., … Tanaka, K. (2010). MMXD, a TFIIH-Independent XPD-MMS19 Protein Complex Involved in Chromosome Segregation. Molecular Cell, 39(4), 632–640. https://doi.org/10.1016/j.molcel.2010.07.029

Kesten, C., Schneider, R., & Persson, S. (2016). In vitro Microtubule Binding Assay and Dissociation Constant Estimation. BIO-PROTOCOL. https://doi.org/10.21769/bioprotoc.1759

Larochelle, S., Pandur, J., Fisher, R. P., Salz, H. K., & Suter, B. (1998). Cdk7 is essential for mitosis and for in vivo Cdk-activating kinase activity. Genes and Development, 12(3), 370–381. https://doi.org/10.1101/gad.12.3.370

Leary, A., Sim, S., Nazarova, E., Shulist, K., Genthial, R., Yang, S. K., … Vogel, J. (2019). Successive Kinesin-5 Microtubule Crosslinking and Sliding Promote Fast, Irreversible

823   Formation of a Stereotyped Bipolar Spindle. *Current Biology*.
824   https://doi.org/10.1016/j.cub.2019.09.030

825   Lee, T., & Luo, L. (2001). Mosaic analysis with a repressible cell marker (MARCM) for
826   Drosophila neural development. Trends in Neurosciences. https://doi.org/10.1016/S0166-
827   2236(00)01791-4

828   Lee, M. J., Gergely, F., Jeffers, K., Peak-Chew, S. Y., & Raff, J. W. (2001). Msps/XMAP215
829   interacts with the centrosomal protein D-TACC to regulate microtubule behaviour. Nature
830   Cell Biology, *3*, 643–649.

831   Lee, C. Y., Andersen, R. O., Cabernard, C., Manning, L., Tran, K. D., Lanskey, M. J., … Doe, C. Q.
832   (2006). Drosophila Aurora-A kinase inhibits neuroblast self-renewal by regulating aPKC/Numb
833   cortical polarity and spindle orientation. *Genes and Development*.
834   https://doi.org/10.1101/gad.1489406

835   Li, X., Urwyler, O., & Suter, B. (2010). Drosophila Xpd regulates Cdk7 localization, mitotic
836   kinase activity, spindle dynamics, and chromosome segregation. *PLoS Genetics*.
837   https://doi.org/10.1371/journal.pgen.1000876

838   Miller, K. E., & Suter, D. M. (2018). An integrated cytoskeletal model of neurite outgrowth.
839   *Frontiers in Cellular Neuroscience*. https://doi.org/10.3389/fncel.2018.00447

840   Minguez, P., Letunic, I., Parca, L., & Bork, P. (2013). PTMcode: A database of known and
841   predicted functional associations between post-translational modifications in proteins.
842   Nucleic Acids Research. https://doi.org/10.1093/nar/gks1230

843   Mirigian, M., Mukherjee, K., Bane, S. L., & Sackett, D. L. (2013). Measurement of In vitro
844   microtubule polymerization by turbidity and fluorescence. Methods in Cell Biology, 115, 215–
845   229. https://doi.org/10.1016/B978-0-12-407757-7.00014-1

846   Moon, H. M., Youn, Y. H., Pemble, H., Yingling, J., Wittmann, T., & Wynshaw-Boris, A. (2014).
847   LIS1 controls mitosis and mitotic spindle organization via the LIS1-NDEL1-dynein complex.
848   *Human Molecular Genetics*. https://doi.org/10.1093/hmg/ddt436

849   Nag, R., Niggli, S., Sousa-Guimaraes, S., Vazquez-Pianzola, P., & Suter, B. (2018). Mms19 is a
850   mitotic gene that permits Cdk7 to be fully active as a Cdk-activating kinase. *Development*,
851   *145*(2).

852   Needleman, S. B., & Wunsch, C. D. (1970). A general method applicable to the search for
853   similarities in the amino acid sequence of two proteins. Journal of Molecular Biology.
854   https://doi.org/10.1016/0022-2836(70)90057-4

855   Paul, V. D., & Lill, R. (2015). Biogenesis of cytosolic and nuclear iron-sulfur proteins and their
856   role in genome stability. Biochimica et Biophysica Acta - Molecular Cell Research.
857   https://doi.org/10.1016/j.bbamcr.2014.12.018

858   Pearson, C. G., & Bloom, K. (2004). Dynamic microtubules lead the way for spindle positioning.
859   *Nature Reviews Molecular Cell Biology*. https://doi.org/10.1038/nrm1402

860   Prakash, L., & Prakash, S. (1977). Isolation and characterization of MMS-sensitive mutants of
861   Saccharomyces cerevisiae. Genetics.

862 Prakash, L., & Prakash, S. (1979). Three additional genes involved in pyrimidine dimer removal
863 in Saccharomyces cerevisiae: RAD7, RAD14 and MMS19. MGG Molecular & General Genetics.
864 https://doi.org/10.1007/BF00333097

865 Rolls, M. M., Albertson, R., Shih, H. P., Lee, C. Y., & Doe, C. Q. (2003). Drosophila aPKC
866 regulates cell polarity and cell proliferation in neuroblasts and epithelia. *Journal of Cell*
867 *Biology*. https://doi.org/10.1083/jcb.200306079

868 Royle, S. J. (2012). The role of clathrin in mitotic spindle organisation. Journal of Cell Science.
869 https://doi.org/10.1242/jcs.094607

870 Sainath, R., & Gallo, G. (2014). Cytoskeletal and signaling mechanisms of neurite formation.
871 Cell and Tissue Research. https://doi.org/10.1007/s00441-014-1955-0

872 Schindelin, J., Arganda-Carreras, I., Frise, E., Kaynig, V., Longair, M., Pietzsch, T., … Cardona,
873 A. (2012). Fiji: an open-source platform for biological-image analysis. *Nature Methods*, *9*, 676–
874 682.

875 Schuldt, A. J., Adams, J. H. J., Davidson, C. M., Micklem, D. R., Haseloff, J., St. Johnston, D., &
876 Brand, A. H. (1998). Miranda mediates asymmetric protein and RNA localization in the
877 developing   nervous   system.   *Genes   and   Development*.
878 https://doi.org/10.1101/gad.12.12.1847

879 Sharp, D. J., Kuriyama, R., Essner, R., & Baas, P. W. (1997). Expression of a minus-end-directed
880 motor protein induces Sf9 cells to form axon-like processes with uniform microtubule polarity
881 orientation. Journal of Cell Science, 110 (19), 2373-80

882 Stehling, O., Vashisht, A. A., Mascarenhas, J., Jonsson, Z. O., Sharma, T., Netz, D. J. A., … Lill,
883 R. (2012). MMS19 assembles iron-sulfur proteins required for DNA metabolism and genomic
884 integrity. Science. https://doi.org/10.1126/science.1219723

885 Van Horn, R. D., Chu, S., Fan, L., Yin, T., Du, J., Beckmann, R., … Ye, X. S. (2010). Cdk1 activity
886 is required for mitotic activation of Aurora A during G 2/M transition of human cells. Journal
887 of Biological Chemistry. https://doi.org/10.1074/jbc.M110.141010

888 Van Wietmarschen, N., Moradian, A., Morin, G. B., Lansdorp, P. M., & Uringa, E. J. (2012). The
889 mammalian proteins MMS19, MIP18, and ANT2 are involved in cytoplasmic iron-sulfur cluster
890 protein assembly. Journal of Biological Chemistry. https://doi.org/10.1074/jbc.M112.431270

891 Vashisht, A. A., Yu, C. C., Sharma, T., Ro, K., & Wohlschlegel, J. A. (2015). The association of
892 the xeroderma pigmentosum group D DNA helicase (XPD) with transcription factor IIH is
893 regulated by the cytosolic iron-sulfur cluster assembly pathway. Journal of Biological
894 Chemistry, 290(22), 14218–14225. https://doi.org/10.1074/jbc.M115.650762

895 Weon, J. L., Yang, S. W., & Potts, P. R. (2018). Cytosolic Iron-Sulfur Assembly Is Evolutionarily
896 Tuned   by   a   Cancer-Amplified   Ubiquitin   Ligase.   Molecular   Cell.
897 https://doi.org/10.1016/j.molcel.2017.11.010

898 Williams, B. C., Riedy, M. F., Williams, E. V., Gatti, M., & Goldberg, M. L. (1995). The Drosophila
899 kinesin-like protein KLP3A is a midbody component required for central spindle assembly and
900 initiation of cytokinesis. Journal of Cell Biology. https://doi.org/10.1083/jcb.129.3.709

901 Yang, Y., Liu, M., Li, D., Ran, J., Gao, J., Suo, S., … Zhou, J. (2014). CYLD regulates spindle
902 orientation by stabilizing astral microtubules and promoting dishevelled-NuMA-dynein/

903   dynactin complex formation. Proceedings of the National Academy of Sciences of the United
904   States of America. https://doi.org/10.1073/pnas.1319341111

905   Yeom, E., Hong, S. T., & Choi, K. W. (2015). Crumbs interacts with Xpd for nuclear division
906   control in Drosophila. *Oncogene*. https://doi.org/10.1038/onc.2014.202

907   Zhou, Y., Yang, S., Mao, T., & Zhang, Z. (2015). MAPanalyzer: A novel online tool for analyzing
908   microtubule-associated proteins. Database. https://doi.org/10.1093/database/bav108

909   Zhu, Z. C., Gupta, K. K., Slabbekoorn, A. R., Paulson, B. A., Folker, E. S., & Goodson, H. V. (2009).
910   Interactions between EB1 and microtubules: Dramatic effect of affinity tags and evidence for
911   cooperative behavior. Journal of Biological Chemistry, 284(47), 32651–32661.
912   https://doi.org/10.1074/jbc.M109.013466

913

914   **Figure Legends**

915

916   Figure 1. ***Mms19^P brains display a microcephaly (small brain) phenotype.*** 3rd instar larval

917   brain NBs were visualized by staining for Miranda (red, cytoplasmic) and pH3 (white,

918   nuclear); DNA (Hoechst 33342 dye) is shown in blue. (A)-(C) A WT brain lobe can be

919   subdivided into the OL (shaded green) and the CB (shaded red). *Mms19^P* brains appear

920   smaller, with a diminished OL. Overexpressing the CAK complex components driven by

921   daughterless-Gal4 (da>CAK) in the *Mms19^P* background did not rescue the phenotype.

922   Mms19::eGFP expressed in the *Mms19^P* background rescued the *Mms19^P* phenotype.

923   Although the number of NBs per brain lobe is similar across all genotypes (D), the volume of

924   the brain lobe is significantly reduced in the *Mms19^P* and da>CAK, *Mms19^P* brains (E).

925   Furthermore, segmentation and volume measurement of the OL and CB revealed a

926   significant reduction in *Mms19^P* and da>CAK, *Mms19^P* brains. The brain volume and

927   morphology were restored to WT levels when Mms19::eGFP was expressed in *Mms19^P*

928   brains (E)-(G). n=15 (15 brains, 30 lobes). Statistical significance (SS) was determined by the

929   Kruskal-Wallis test. Multiple columns were compared using Dunn's posttest, ***(*P*<0.001),

930   scale=25μm.

931

932   Figure 2. **NBs depend on *Mms19* for timely and coordinated spindle assembly and spindle

933   orientation.** (A) WT NBs typically finish cytokinesis 10 min after the onset of nuclear

934   envelope breakdown (NEBD). (B) *Mms19^P* NBs require on average 20 min to reach

935   cytokinesis after NEBD. (B, B') In around 10% the mutant cells, the spindle poles are not fully

936   separated at NEBD and the spindle initially appears kinked. In around 20% of *Mms19^P* NBs,

937   the spindles change their orientation throughout the course of mitosis. (C) In this particular

938   mutant case, MTs are initially seen to emanate only from a single pole, but subsequently,

939   the other pole also nucleates MTs. The quantitative assessment of the duration of WT and

940   *Mms19^P* mitoses is compared in (D). SS was determined by an unpaired t-test (***P*<0.001);

941   Scale=5μm; n=30 NBs. Kinked spindles and mis-oriented spindles are quantified in (E).

942

943   Figure 3: ***Mms19* is required to form a spindle of normal length and density.**

944   (A-A') Z projection of a typical bipolar spindle in a WT NB with the spindle poles anchored to

945   the cell cortex. (B-B') short spindle found in *Mms19^P* NBs. the spindle is abnormally short

946   and the spindle poles are detached from the cortex. (C) WT spindles are significantly longer

947   than *Mms19^P* and da>CAK, *Mms19^P* spindles. (D) Graph comparing cell diameters between

948   the different genotypes. WT NBs are bigger than *Mms19^P* and da>CAK, *Mms19^P* cells. (E) In

949   order to quantify the short spindles, I normalized the spindle lengths to the cell diameters. If

950   this ratio was equal to or less than 0.6, I considered these as 'short spindles'. (F) Graph

951   comparing the percentage of 'short spindles' across different genotypes. n= 90 NBs.

952   Relative density of astral MTs was quantified and compared across all genotypes. Maximum

953   intensity projections of mitotic NBs were obtained and the relative density of astral MTs was

954   quantified as shown in (G). (H) Astral MT density and (I) Inner spindle fluorescent intensity

955   was measured in fixed NBs immunostained for αTubulin and compared across all the

956   genotypes n= 60 NBs. SS was calculated using Kruskal-Wallis test, columns were compared

957   using Dunn's post test (****P*<0.0001, ****P*<0.001; ***P*<0.01, **P*<0.05), scale=5μm.

958

959   Figure 4. ***Mms19* assists MT polymerization *in vivo*.** (A) WT and *Mms19^P* NBs expressing

960   EB1::GFP were imaged live and time-lapse movies were acquired to calculate the velocity of

34

961   EB1::GFP labelled MT 'plus' ends. The velocities represented in (A') show reduced MT

962   growth velocity in *Mms19^P* NB spindles. n=11 cells, 5 particles analyzed from each cell (B-B')

963   EB1::GFP velocities were compared across WT and *Mms19^P* in the glia. SS for A' and B' was

964   calculated using unpaired t-test, (**$P<0.01$) (***$P<0.001$), scale bar=5μm. n=15 brains, 10

965   particles analyzed from each brain (C) In a WT NB, a spindle is seen to be fully assembled

966   approximately 3 minutes after NEBD. (D) On the other hand, in most *Mms19^P* NBs, spindle

967   assembly seemed to be delayed.

968

969   Figure 5. ***Mms19* is required for spindle re-polymerization.** After cold treatment, spindle re-

970   assembly was analyzed at 0 sec (i.e. immediately after cold treatment; left panel), 30 sec

971   (central panel) and 90 sec (right panel) after shifting them to 25°C. At 0 sec in the WT (A),

972   only the centrosomes were visible but after incubation at 30 sec a few fibers nucleated from

973   the centrosomes. At 90 sec, the spindle regained its normal shape. In *Mms19^P* NBs (B),

974   spindles did not regain the normal shape after 90 sec. Additionally, the microtubule density

975   was reduced in the stunted spindles. Expression of Mms19::eGFP in the mutant background

976   (C), rescued spindle reformation, but overexpression of CAK (D) rescued only partially and

977   the length and density of MT still appeared reduced. (E) Chart comparing length of spindles

978   after 90 sec incubation at 25°C. (F) The box plot (G) shows the spindle length relative to the

979   cell diameter, thus eliminating variations due to varying cell sizes. SS was calculated by

980   Kruskal-Wallis test, columns were compared by Dunn's posttest (***$P<0.001$), scale=5μm,

981   n=60 (F) The graph compares the percentage of 'short spindles' across different genotypes.

982

983   Figure 6. **Centrosomal localization of the MT regulator TACC depends on Mms19.** (A) A

984   mitotic NB shows TACC localization at the spindle poles. (B, D) >50% of analyzed *Mms19^P*

985   NBs fail to localize TACC to spindle poles. (C, D) TACC localization was restored upon

986   overexpression of the CAK subunits Cdk7, CycH and Mat1 in the *Mms19^P* background. (E)

987   The amount of TACC localized on the centrosomes was quantified by comparing the

988   fluorescent intensity of the centrosomal TACC signal to the TACC signal on the spindles. A

989   ratio greater than 1 was considered as clear centrosomal TACC, while a ratio equal to or less

990   than 1 indicated unlocalized TACC. SS was calculated by Kruskal-Wallis test, columns were

991   compared by Dunn's posttest (***$P<0.001$), scale=5μm. n=60 NBs. (F, G) NBs were stained

992   with antibodies against γTubulin to test for centrosomal localization. (G) TACC co-colocalized

993   with γTubulin on the centrosomes. (F) In the mutant NB TACC fails to concentrate at

994   γTubulin foci.

995

996   Figure 7. **Mms19::5xHis binds to tubulin and stimulates MT assembly *in vitro*.** Mms19-

997   Tubulin interaction using a pull-down assay performed at 4°C. Purified tubulin and

998   Mms19::5xHis were first incubated at equimolar ratios and subsequently with Ni-NTA resin

999   which binds His-tags. (A) Input panels show Tubulin added, either alone or with Mms19. (B)

1000   Tubulin was found binding to the resin only upon prior incubation with Mms19::5xHis.

1001   Tubulin added alone did not bind to the resin. (C) Purified Mms19 was incubated with

1002   tubulin in the presence of GTP and the absorbance was measured at 340nm at 35°C to

1003   assess polymerization. MAPF (Cytoskeleton Inc.) was used as a positive control, whereas

1004   Mms19 alone and tubulin with solvent (the solvent in which Mms19 was reconstituted)

1005   were used as negative controls. (D-D') Absorbance of MTs increases when incubated with

1006   Mms19, but sharply decreases after incubating this mixture on ice for 10 minutes. (E) MTs

1007   only (without Mms19::5xHis added) visualized by negative stain EM. Here, a MT fiber can be

1008   seen depolymerizing (indicated by arrow). (F) In a Mms19::5xHis-MT mixture, discreet
1009   particles can be seen binding laterally along the surface of MT. (G) Measuring the length of
1010   MT fibers revealed that MTs were generally longer when incubated with Mms19::5xHis and
1011   tubulin, compared to tubulin to which only the BRB80/solvent buffer was added. n=150
1012   MTs, ss was calculated using unpaired t-test, ****p<0.0001. MT bundles containing 2 (H) or
1013   more than 2 MTs (I) were more frequently observed upon addition of Mms19::5xHis to MTs.
1014

Supporting Information legends

Supporting Figures

Figure S1: Higher fraction of Mms19P NBs in mitosis. (A) NBs were classified into 1) G1/G0 phase if they did not stain for either EdU or pH3; 2) S phase if the NBs stained positively for EdU; 3) M phase for NBs staining positively only for pH3 and 4) G2/M for cells staining positively for both EdU and pH3. The G2/M cells are cells transitioning from G2 to M phase. NBs in each phase were counted per brain lobe and this data was represented as percentage (e.g. if in one brain lobe 20 out of 100 NBs were pH3 positive, then 20% cells were classified as in M phase). The percentages for each phase were compiled and compared per brain lobe across the 4 genotypes. Box plot charts represent percentage of cells in (B) G1/G0 phase, (C) S phase and (D) G2/M phase. (E) M phase. 30 brain lobes per genotype were analyzed. SS was calculated using Kruskal-Wallis test, columns compared using Dunn's post test, ***($P<0.001$), *($P<0.05$). Scale=5μm.

Figure S2: *Mms19* is cell autonomously required to maintain normal cell numbers in MARCM clones. (A)-(C) In order to study cell cycle progression in a single NB lineage, we used the Mosaic Analysis with a Repressible Cell Marker (MARCM) technique (Lee and Luo, 2001). This technique utilizes the UAS-GAL4-GAL80 system and the FLP-FRT recombination system. With this technique, a population of cells arising from the same progenitor can be specifically labeled. Additionally, the progenitor cell can carry a mutation along with a GFP marker. Defects in this cell, along with its progeny can be analyzed in an otherwise WT background. (E) MARCM clones were induced in NBs in 24hrs old larvae. These larvae were dissected after another 48hrs to determine the number of cells per clone in *Mms19P* and WT/control clones. (F) The graph shows a significant reduction in numbers of cells in mutant clones. SS was determined by an unpaired t-test (**$P<0.01$), scale=5μm, n=60 clones from each genotype.

Figure S3: Model for mitotic and post-mitotic pathways of Mms19. (A) Mms19 binds to Xpd, thereby releasing the CAK complex to activate its mitotic targets. (B) Downregulation of Mms19 by mutations, knock-down or proteasome mediated degradation allows Xpd to associate with CAK and core TFIIH, thereby targeting Cdk7 activity away from the mitotic targets and towards transcriptional targets like the PolII- CTD (Cameroni et al, 2010). (C) Mms19 binds to MTs and promotes MT stability and bundling, contributing significantly to establishing extended MT structures such as mitotic spindles and possibly the MTs driving neurite outgrowth.

Figure S4: *Mms19P* NBs show spindle orientation defects. (A) Spindle orientation in the WT NBs is tightly coupled to the apical-basal polarity axis. (B) In a fraction of *Mms19P* NBs the spindle appears mis-oriented with respect to the Mira crescent localization. (D-E) Quantification of the spindle angle revealed that a considerably higher number of *Mms19P* NBs are oriented at an angle of more than 10° w.r.t Mira. n=65, scale=5μm.

Figure S5: *Mms19P* NBs do not display high levels of aneuploidy. (A) WT, *Mms19P* and da>CAK, *Mms19P* brains were fixed and fluorescent *in situ* hybridization was performed on them. Cy5-labelled DNA probes that specifically bind to regions on the 2nd chromosome were used to determine the number of chromosomes. (A) the signal is seen as 2 dots in the WT NBs corresponding to the diploid state of the cell. (B) An example of an aneuploid *Mms19P* NB showing 3 dots. (C) However, aneuploid cells in both *Mms19P* and da>CAK, *Mms19P* NBs were extremely rare. SS was calculated using Fisher's exact test.

Figure S6: *Mms19* is necessary for centrosomal localization of Msps in NBs. (A, C) WT and da>CAK, *Mms19P* NBs showing Msps localization on centrosomes and spindles. (B) In *Mms19P*

NBs, Msps does not concentrate on centrosomes. (D) To quantify centrosomal accumulation of Msps, an analysis similar to that done in Fig 6 was performed. SS was calculated using Kruskal-Wallis test, columns compared using Dunn's post test, ***(P<0.001), scale=5μm, n=30.

Figure S7: Putative ubiquitination site in *Drosophila* Mms19: A pairwise sequence alignment of the human MMS19 and *Drosophila* Mms19. The alignment performed was based on the Needleman-Wunsch algorithm (Needleman and Wunsch, 1970; https://www.ebi.ac.uk/Tools/psa/emboss_needle/). Analysis of both sequences by the PTMcode 2 software indicates that the C-terminal K993 site in the Human protein is conserved in the *Drosophila* Mms19 at K921.

Figure S8: *Mms19P* neurons are unable to form long neurites in culture. (A) WT NBs differentiated into neurons and extended neurites after 24hrs in culture. Neurons were positive for Elav (marker for post mitotic neuronal nuclei). (B) *Mms19P* neurons stained positively for Elav after 24hrs in culture, indicating that these neurons had differentiated. (C) *Mms19P* neurons, did not grow extended neurites after 24hrs or even (D) 48hrs in culture. Scale bar=5μm.

Supporting Tables

Supplementary Table 1. The table lists proteins found to exclusively co-purify with Mms19::eGFP. CIA proteins, which are already known to form a complex with Mms19, are highlighted in Red. Microtubule associated proteins are highlighted in Green.

Supplementary Table 2. Proteins that bound to the anti-GFP antibody coated beads from all three fly extracts are listed. These include different isoforms of α-and βtubulin that were identified in all extracts. However, the PMSS scores are higher for the tubulin isoforms immuno-precipitating from the Mms19::eGFP extract. This indicates that tubulin was enriched in the Mms19::eGFP fraction compared to the wild-type control.

Supporting Movies

Mov 01:

Analysis of mitosis duration in WT NB: WT brains expressing EB1::GFP were dissected, mounted on a stainless steel chamber (Cabernard et al, 2013) and NB mitosis was imaged with a 63x objective on a spinning disk confocal microscope. Mitosis duration was measured from NEBD onset (start at 0 min) until cytokinesis. Scale=5μm

Mov 02:

Analysis of mitosis duration in *Mms19P* NB: Mitosis was visualized in *Mms19P* brain NBs expressing EB1::GFP. On average, *Mms19P* brain NBs took twice as long as WT NBs to finish mitosis. In this presented case, the NB completes mitosis 22min after NEBD onset with cytokinesis. Scale=5μm

Mov 03:

Spindle assembly defect in *Mms19^P* NB: In around 10% of EB1::GFP expressing *Mms19^P* brain NBs, the spindle starts assembling before the centrosomes have migrated to the opposite sides, forming a 'kinked' spindle at 4min post NEBD onset. This indicates that Mms19 is needed for coordinating spindle formation with cell cycle progression. Scale=5µm

Mov 04:

Analysis of EB1::GFP labelled MT velocity in WT NBs: In order to determine the speed of growing MT tips, WT brains expressing EB1::GFP were dissected, mounted on a stainless steel chamber (Cabernard et al, 2013) and spindles were imaged with a 100x objective on a spinning disk confocal microscope. Images were acquired at an interval of 500ms for 1min. Scale=5µm.

Mov 05:

Analysis of EB1::GFP labelled MT velocity in *Mms19^P* NBs: Live imaging was performed on *Mms19^P* brain NB spindles to determine the velocity of growing MT tips. Images were acquired at an interval of 500ms for 1min. The spindle shown here appears to tilt repeatedly, perhaps due to defects in astral MT assembly (Fig 2, Fig 6). Scale=5µm.

Mov 06:

Measuring MT plus tip speeds in post mitotic surface glia of WT brains: In order to determine whether *Mms19* affects MT growth in post mitotic cells, WT brains expressing EB1::GFP were dissected, mounted on a stainless steel chamber (Cabernard et al, 2013) and MT growth in surface glia was imaged with a 100x objective on a spinning disk confocal microscope. Images were acquired at an interval of 500ms. Scale=5µm.

Mov 07:

Measuring MT plus tip speeds in post mitotic surface glia of *Mms19^P* brains: MT growth in EB1::GFP expressing *Mms19^P* surface glia was visualized using spinning disk confocal microscopy. Images were acquired at an interval of 500ms. Scale=5µm.

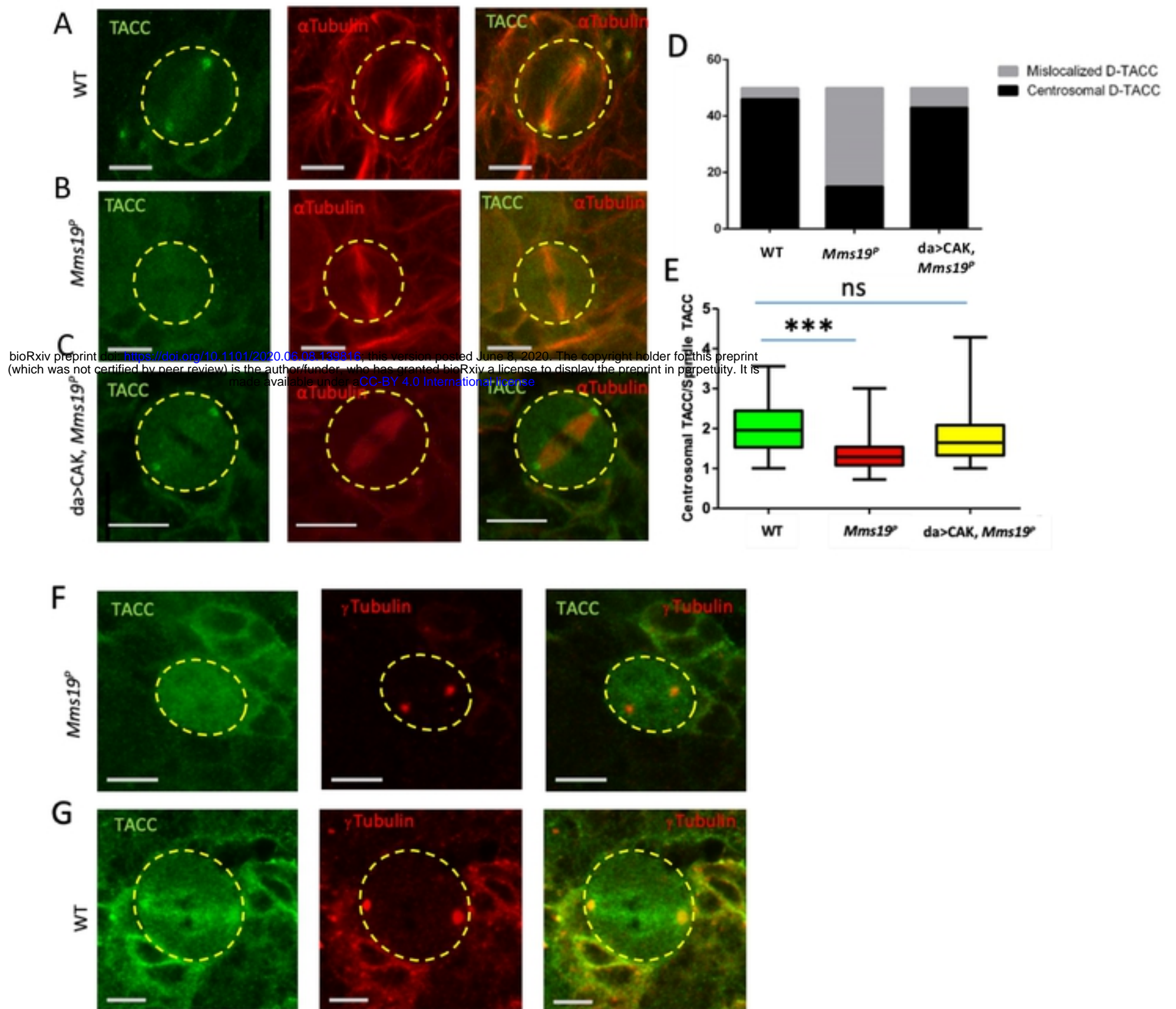# Figure 6: Centrosomal localization of the MT regulator TACC depends on Mms19

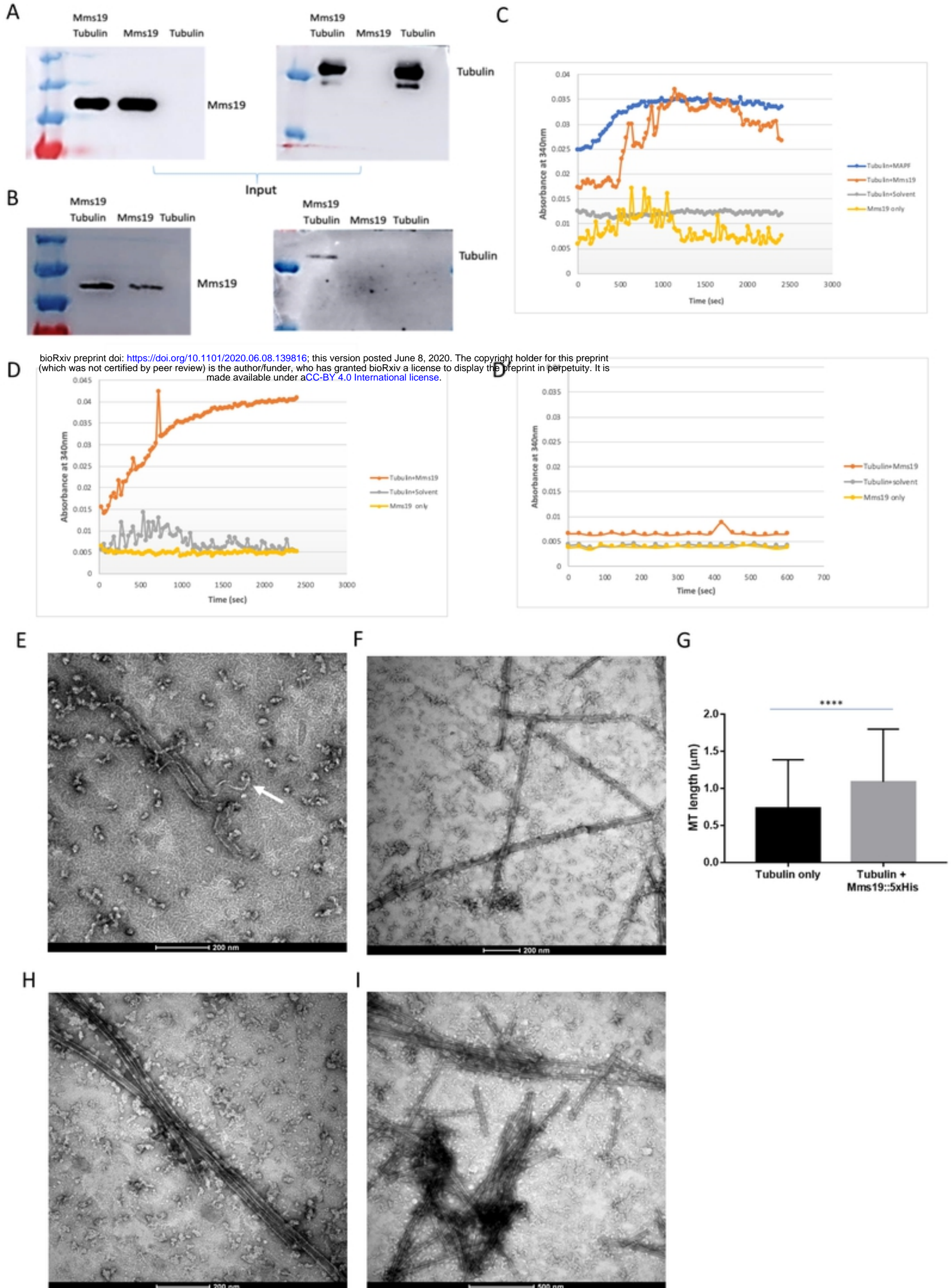# Figure 7:Mms19 binds to tubulin and stimulates MT assembly *in vitro*.

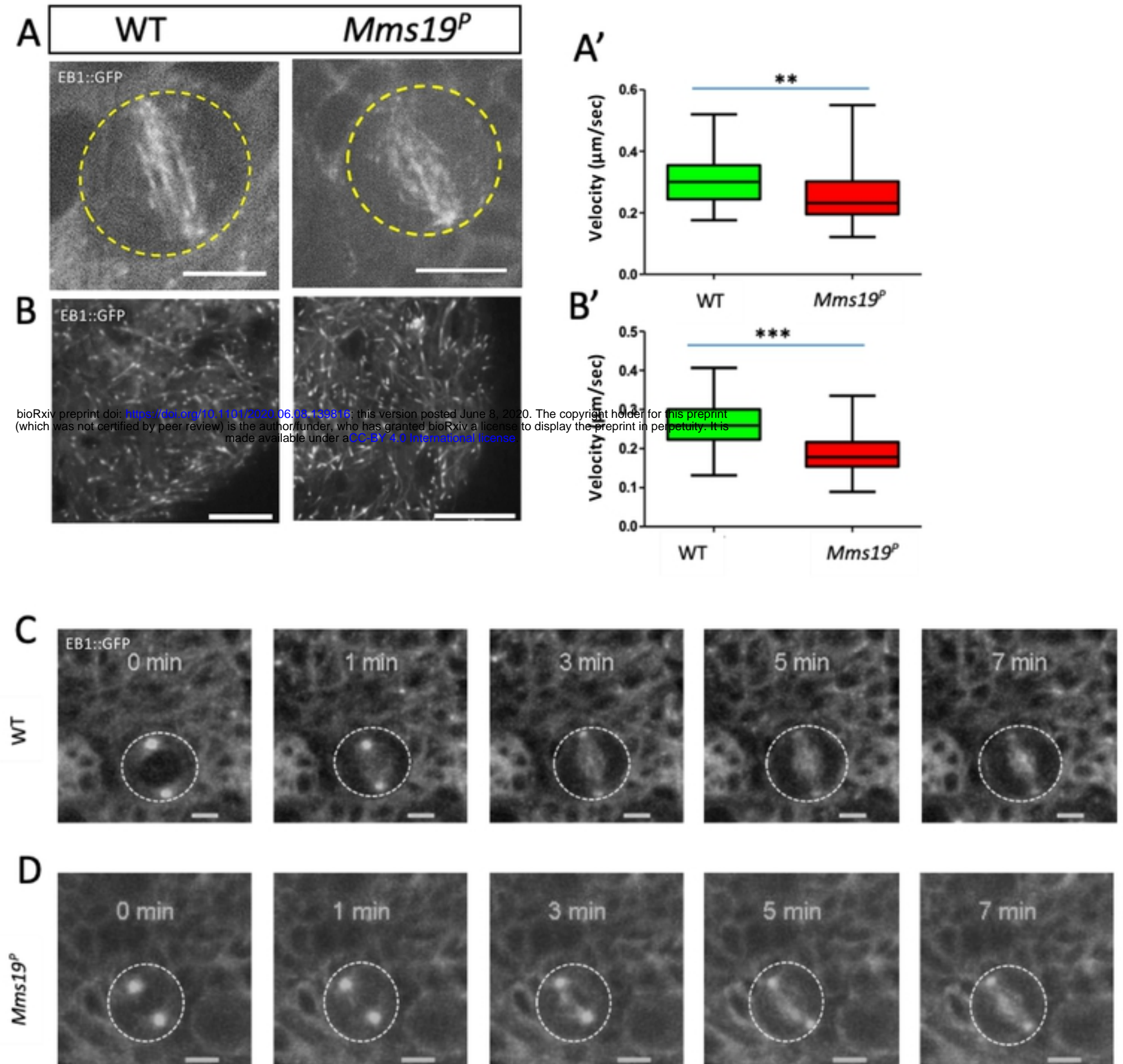# Figure 4: *Mms19* assists MT polymerization *in vivo*.

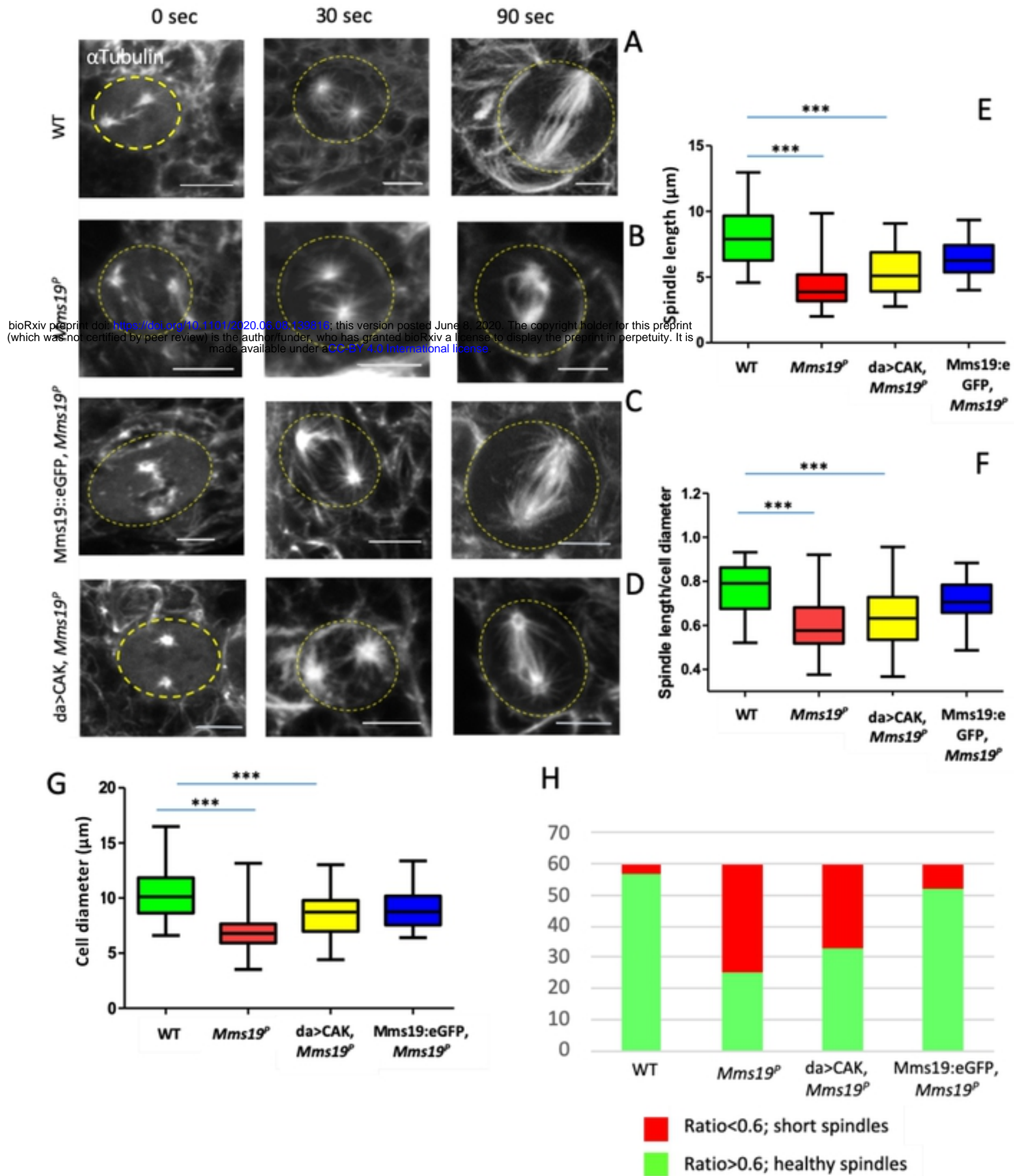# Figure 5: *Mms19* is required for spindle re-polymerization.

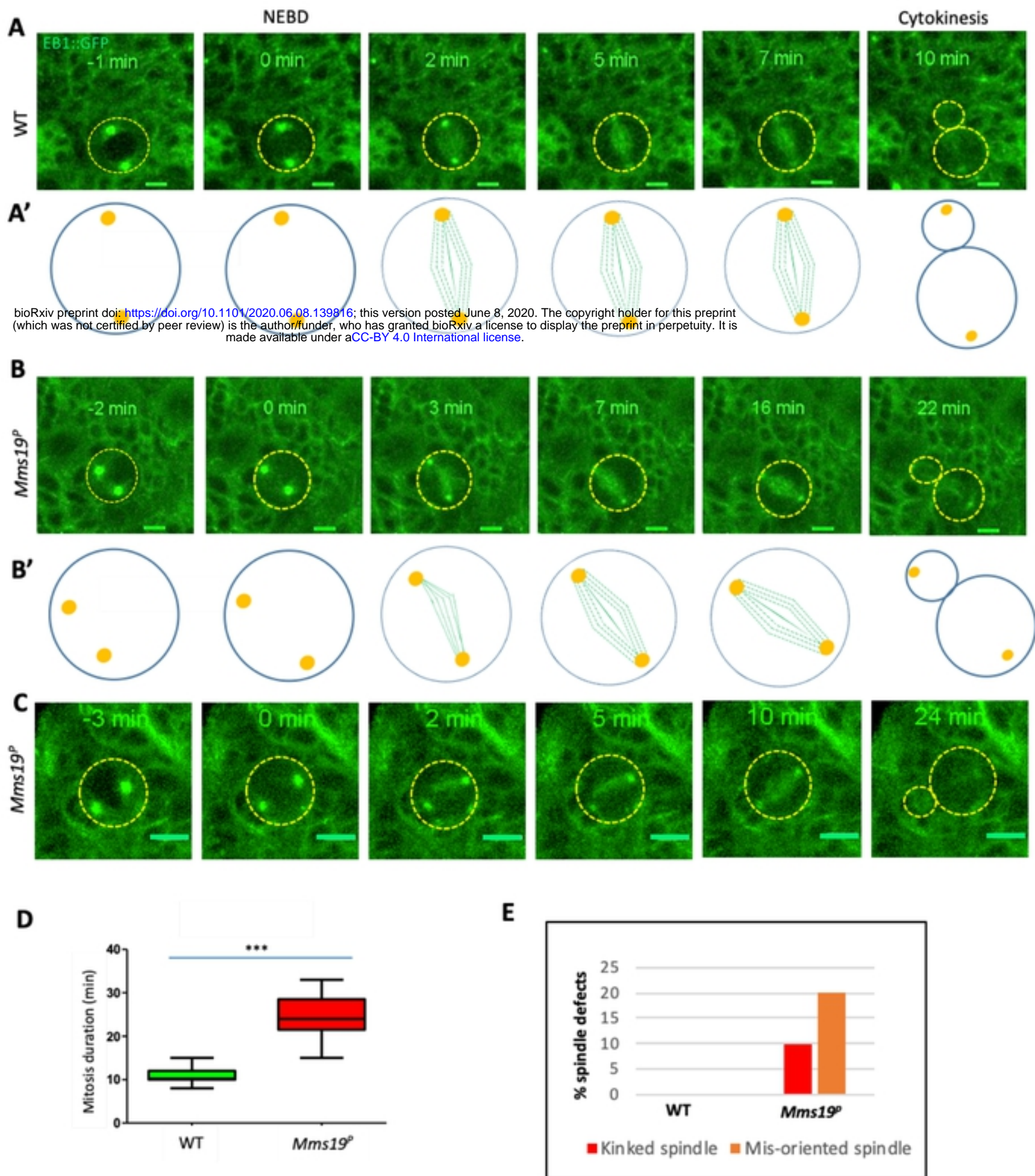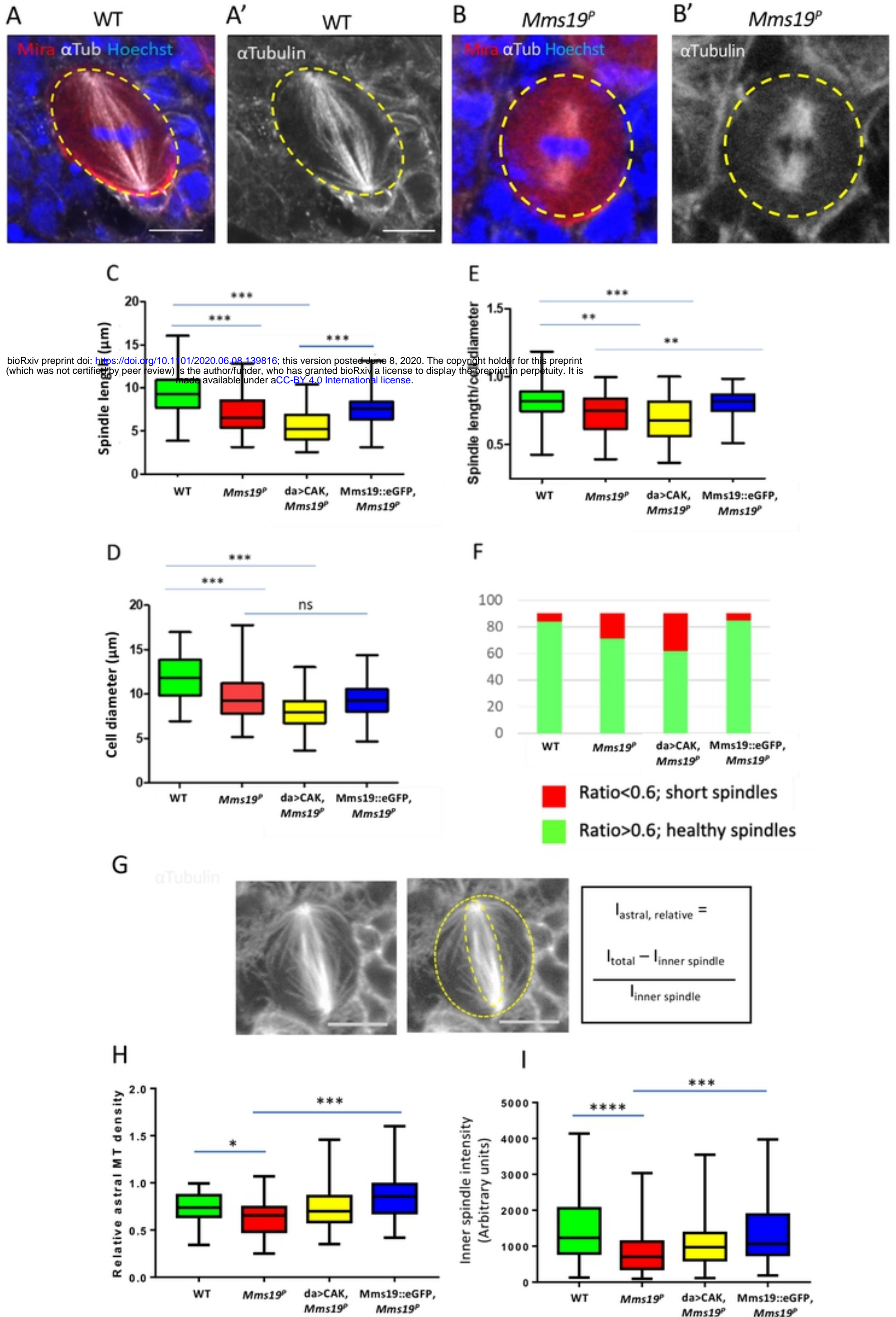# Figure 2: Neuroblasts depend on *Mms19* for timely and coordinated spindle assembly and spindle orientation

Figure 3: *Mms19* is required to form a spindle of normal length and density

Figure 1: *Mms19^P* brains show a microcephaly (small brain) phenotype

Figure 1